UC Davis
UC Davis Previously Published Works

Title

Synchronization of Electrically Coupled Resonate-and-Fire Neurons.

Permalink

https://escholarship.org/uc/item/8336q2bs

Journal

SIAM journal on applied dynamical systems, 18(3)

ISSN

1536-0040

Authors

Chartrand, Thomas
Goldman, Mark S
Lewis, Timothy J

Publication Date

2019

DOI

10.1137/18m1197412

Peer reviewed

Synchronization of Electrically Coupled Resonate-and-Fire Neurons

Thomas Chartrand[†], **Mark S. Goldman**[‡], **Timothy J. Lewis**[§]

[†]Graduate Group in Applied Mathematics, University of California-Davis, Davis, CA 95616. Current address: Allen Institute for Brain Science, Seattle, WA.

[‡]Center for Neuroscience, Department of Neurobiology, Physiology and Behavior, Department of Ophthalmology and Vision Science, and Graduate Group in Applied Mathematics, University of California-Davis, Davis, CA 95616.

[§]Department of Mathematics and Graduate Group in Applied Mathematics, University of California-Davis, Davis, CA 95616.

Abstract

Electrical coupling between neurons is broadly present across brain areas and is typically assumed to synchronize network activity. However, intrinsic properties of the coupled cells can complicate this simple picture. Many cell types with electrical coupling show a diversity of post-spike subthreshold fluctuations, often linked to subthreshold resonance, which are transmitted through electrical synapses in addition to action potentials. Using the theory of weakly coupled oscillators, we explore the effect of both subthreshold and spike-mediated coupling on synchrony in small networks of electrically coupled resonate-and-fire neurons, a hybrid neuron model with damped subthreshold oscillations and a range of post-spike voltage dynamics. We calculate the phase response curve using an extension of the adjoint method that accounts for the discontinuous post-spike reset rule. We find that both spikes and subthreshold fluctuations can jointly promote synchronization. The subthreshold contribution is strongest when the voltage exhibits a significant post-spike elevation in voltage, or plateau potential. Additionally, we show that the geometry of trajectories approaching the spiking threshold causes a "reset-induced shear" effect that can oppose synchrony in the presence of network asymmetry, despite having no effect on the phase-locking of symmetrically coupled pairs.

Keywords

resonate-and-fire model; synchronization; electrical coupling; gap junction; phase response curve; hybrid model

AMS subject classifications.

92B25; 34D06; 34C15; 34C20; 92C20; 34A38; 37G15; 37N25

tom.chartrand@alleninstitute.org.

1. Introduction.

Synchronization of activity between neurons has been hypothesized to contribute to a variety of brain functions [99], including motor control [25], memory [41], and coordination between brain regions [14]. This synchrony can be supported by either electrical or chemical synapses, or some combination of the two. Because electrical synapses (gap junctions) diffusively couple the voltages of connected cells, their effect is typically thought to be synchronizing, an idea with support from both theoretical and experimental studies [7, 19, 74]. However, their effect is potentially more complex, and exceptions to this rule have been noted [97, 18, 69]. In part, this is because the coupling combines effects at the dramatically different timescales of spiking activity and subthreshold fluctuations of membrane potential [69, 18, 89]. Subthreshold voltage dynamics can vary dramatically across different cell types, particularly in resonant cells that are often electrically coupled, and these variations can affect synchronization mediated by electrical synapses [18, 89, 74, 27]. The resonant properties that determine a frequency-selective spiking response to input also cause subthreshold dynamics such as transient oscillations, hyperpolarization followed by rebound, or a depolarized plateau following the spike [51]. Our goal is to explore the interaction between electrical coupling and resonant intrinsic dynamics of spiking neurons to understand both the dynamical mechanisms involved and their relevance to the function of neural systems, including showing how synchronization can vary between resonant neurons with different patterns of subthreshold voltage.

We study the effect of electrical coupling on the synchronization of resonant spiking neurons by applying the theory of weakly coupled oscillators to reduce the complexity of the synchronization problem and gain analytical insight [5]. This technique relies on a perturbative approximation to derive a reduced *phase model* for limit cycle oscillators [96]. Synchronization of the phase model is determined by the *interaction function*, which captures the effect of coupling as a function of the phase of each oscillator along its periodic limit cycle. Determining how the interaction function depends on a property of the oscillator, such as subthreshold resonance, spike size, or post-spike behavior, shows how that property contributes to synchronization.

Common challenges in phase reduction analysis are that it may not be possible to independently vary the dynamical properties of interest, or to analytically compute the interaction function. To address these challenges, we use an idealized hybrid neuron model for the dynamics of resonant spiking. Hybrid neuron models, such as the integrate-and-fire model and its generalizations, simplify spiking as a threshold crossing with discrete post-spike reset, combined with continuous subthreshold dynamics between spikes. We focus on the resonate-and-fire model [53], which has linear damped oscillations as its subthreshold dynamics to model resonant phenomena. The subthreshold linearity and discrete reset map allow the model to remain analytically tractable and yet capture a wide range of post-spike voltage dynamics, including both plateau potentials (prolonged elevation of voltage) and after-hyperpolarization (AHP), a dip in voltage following the spike. With the separation of discrete and continuous dynamics, we can independently vary the subthreshold and spiking properties of the model and determine their effects on the synchrony of small model networks.

On the other hand, the discrete reset map complicates the application of weakly coupled oscillator theory for the analysis of synchrony. Calculating the *phase response curve* (PRC), which measures the phase shift resulting from a perturbation to the oscillator at any point along the limit cycle, is the first step in the phase model reduction. The discontinuous spiking dynamics lead to discontinuity of the PRC, which is usually derived under an assumption of continuous periodicity. In certain cases, discontinuous PRCs can be calculated directly [80, 23, 38], but the discontinuity in general necessitates an extension of standard methods for calculating the PRC. Recent results have shown that for general hybrid models the PRC can be calculated by a variation to the standard "adjoint method" [98, 87], linked to the saltation matrix of nonsmooth dynamical systems theory [8, 3]. We present an alternative, intuitive derivation of this result that elucidates the connection to the geometry of the threshold and reset in hybrid neuron models, and we apply this understanding to our resonate-and-fire analysis.

The paper is organized as follows. In section 2, we describe the general properties and history of hybrid models in neuroscience and define the resonate-and-fire model. In section 3, we review the theory of weakly coupled oscillators and present our approach to calculating the PRC for hybrid models. The remainder of the paper contains our analysis of synchronization in the electrically coupled resonate-and-fire model. In section 4, we apply our adjoint method approach to obtain analytical expressions for the PRC and interaction function of the model. To explore the dependence of the interaction function on model parameters, we focus separately on the even- and odd-symmetric components of the interaction function, which lead to distinct effects on synchrony determined by the symmetry of network coupling. In section 5, we show that the spike itself always promotes robust synchrony through its contributions to the odd component, while the post-spike subthreshold fluctuations can additionally strongly promote synchrony in the plateau potential regime. We also show, in section 6, that the threshold and reset can phase-shift the interaction function through "reset-induced shear" arising from the geometry of trajectories crossing the threshold, leading to an even component that can have complex effects on synchronization. In example three-cell networks, the presence of this even component leads to often-ignored effects on network synchronization when heterogeneity of frequencies or coupling breaks the symmetry of the interactions.

2. Hybrid models and the resonate-and-fire model.

Hybrid models have a central role in the history of mathematical neuroscience. Well before the detailed processes generating action potentials were understood, Lapicque [67] postulated that inputs to a neuron accumulate in a continuous process of integration, eventually triggering a spike. This idea led to the leaky integrate-and-fire model (2.1) and a number of variations that are still widely used [35, 53, 54, 10, 1]. The separation of the dramatically different timescales of spiking and subthreshold dynamics into distinct mechanisms gives these models both computational efficiency and analytic tractability. Hybrid models have surprisingly rich and complex dynamics, inspiring active study from both neuroscience and dynamical systems perspectives [104, 95, 15]. We first introduce some fundamental examples of hybrid models in neuroscience and then define the specifics of the resonate-and-fire model along with notation for arbitrary hybrid model dynamics.

2.1. Single-variable integrate-and-fire models.

The leaky integrate-and-fire model consists of a single voltage variable with linear subthreshold dynamics between spikes [67, 13, 1]. External current input I is integrated through changes in the neuron's membrane potential (voltage) subject to a "leak," or linear decay over time (governed by the membrane capacitance C, conductance g_L, and reversal potential v_L). When voltage crosses a threshold v_T from below, a spike occurs, and the voltage is reset to v_R.

$$C\frac{dv}{dt} = -g_L(v - v_L) + I, \; v(t^-) = v_T \Rightarrow v(t^+) = v_R. \tag{2.1}$$

For sufficiently large constant current input, the equilibrium voltage $v_{eq} = v_L + \frac{I}{g_L}$ is pushed over the threshold v_T, and the model exhibits a regular spiking state, a limit cycle with periodic firing. Note that the existence of a limit cycle in one dimension is enabled by the discontinuous reset.

A number of variations on this classic model have been proposed. In a single dimension, nonlinear variants can approximate the effects of voltage-dependent ion channel conductances on subthreshold dynamics, more accurately modeling the approach to threshold. Prominent examples include the quadratic [35, 12] and exponential [42] integrate-and-fire models, as well as arbitrary nonlinearities derived via model reduction or optimized to match recorded spike trains [58]. For the analysis of synchrony, a number of significant theoretical discoveries have been made using networks of single-variable integrate-and-fire neurons coupled by chemical or electrical synapses [36, 78, 63, 21, 44, 69, 89, 85, 70, 73].

Despite these successes, some firing properties of real cells (and of more realistic models) are not captured by single-variable models, particularly fluctuations in subthreshold voltage following the spike. The diversity of post-spike dynamics found in different cell types includes fast (Figure 2.1a left) and slow (Figure 2.1a center) AHP, plateau potentials (Figure 2.1a right), and damped oscillations. Although variations in the level of fast AHP can be modeled to a limited degree in single-variable models [89], the other examples shown cannot be represented due to nonmonotonic voltage trajectories. To capture these requires increasing the dimensionality of the model.

2.2. Multivariable linear integrate-and-fire models.

The idea of linear feedback between two factors governing a neuron's approach to the firing threshold was developed independently by some of the earliest mathematical neuroscientists, Rashevsky [91], Hill [49], and Young [112]. Adding a second "adaptation/facilitation" current variable [105, 92, 77] allows a model to reflect slow recovery processes in the neuron (typically the gating dynamics of ion channels) that can create resonance, adaptation, and a full range of post-spike voltage dynamics.

A multivariable "generalized integrate-and-fire" model can also be derived from a Hodgkin–Huxley-type biophysical model by linearizing and exploiting separation of timescales to eliminate variables [92, 60, 56]. In the simplest example, a single additional variable

captures the most significant slow current, often a calcium, potassium, or hyperpolarization-activated h-current, or a combination of channels with similar time constants. (For higher-dimensional linear models, also see [77, 29, 57, 103].) The subthreshold dynamics of a two-variable linear model with slow current z can be described by [92, 60, 56]

$$
\begin{aligned}
C\frac{dv}{dt} &= -g_L(v - v_L) - z + I, \\
\tau\frac{dz}{dt} &= k(v - v_z) - z.
\end{aligned}
$$

(2.2)

This reduced model, with a suitable reset map included, has been shown to capture realistic spiking dynamics in a range of biologically relevant scenarios [92, 11, 60, 6]. We discuss the details of reset maps in two dimensions below (section 2.4), but for now we simply consider the properties of a limit cycle trajectory with reset point $x_0 = (v_0, z_0)$.

In a two-dimensional model, the reset voltage v_0 can have a strong effect on the shape of the voltage trajectory, reproducing a range of post-spike dynamics as shown in Figure 2.1b. The voltage trace for a model reset below the firing threshold resembles a fast AHP (Figure 2.1b, left), as in the leaky integrate-and-fire model. In contrast, when the subthreshold dynamics have an oscillatory component, v_0 can be reset above threshold to resemble a plateau potential (Figure 2.1b, right) or at the threshold to resemble a slow AHP (Figure 2.1b, center). Additional comparison with these biophysical models is shown in section A.1.

Despite the relevance of these distinct voltage dynamics to electrical synaptic interactions, only a few studies have addressed the synchronization of electrically coupled hybrid models with more than a single variable [23, 22], and none have considered the effects of post-spike fluctuations specifically. We also note that *nonlinear* integrate-and-fire models in multiple dimensions can be remarkably effective at reproducing diverse spiking patterns [100, 54, 55, 10, 82] and have been applied to study synchronization through chemical synapses [26, 20, 79, 80, 38, 64, 65]. However, such nonlinear models are in general not analytically tractable. For this reason, we choose to explore the full range of post-spike dynamics in a linear two-variable integrate-and-fire model that permits direct analysis of synchronization.

2.3. Resonate-and-fire model.

The resonate-and-fire model is a two-dimensional linear integrate-and-fire model introduced by Izhikevich [53] with the goal of capturing essential features of the dynamics of resonant cells. Several studies have examined dynamics of the resonate-and-fire model in biologically relevant scenarios, including spiking triggered by periodic and noisy input [11, 92, 106, 60] and synchronization of pulse-coupled networks [79, 80, 81], and a variation on the model has been used to fit realistic spike train data [17]. Given the rich range of possible dynamics, we choose to analyze synchronization in the resonate-and-fire model rather than a more general two-dimensional linear integrate-and-fire form.

The subthreshold dynamics of the resonate-and-fire model are a slightly restricted canonical form of (2.2) in the damped oscillation regime (complex eigenvalues). Additionally, the model restricts the parameter space by assuming that a single time constant λ governs the

decay of both variables, $\lambda = \frac{g_L}{C} = \frac{1}{\tau}$.[1] To simplify our notation, the slow current variable z is replaced by an effective adaptation/facilitation variable $w = \frac{1}{\Omega C} z$ with $\Omega = \sqrt{\frac{k}{\tau C}}$, voltage is measured relative to v_z, and the tonic current input is subsumed into the equilibrium voltage $v_{eq} = v_L - v_z + \frac{I}{g_L}$;

$$\frac{dv}{dt} = -\lambda(v - v_{eq}) - \Omega w,$$
$$\frac{dw}{dt} = -\lambda w + \Omega v.$$

(2.3)

Without loss of generality, we set the threshold voltage to $v_T = 0$ and rescale time such that $W = 1$ (though allowing variations about this mean frequency in the network setting). Unless otherwise specified, we choose a fixed value for the decay parameter, $\lambda = 0.1$; our results are qualitatively similar as long as λ is sufficiently small (relative to $W = 1$). In the opposite extreme, taking the limit $\lambda \to \infty$ with W fixed recovers the leaky integrate-and-fire model.[2] With these parameters fixed, the equilibrium voltage and details of reset determine the existence and properties of spiking in the model. If a trajectory starting from the reset point x_0 crosses the spiking threshold and is again reset, it forms a spiking limit cycle corresponding to regular spiking, shown in Figure 2.1b and Figure 2.2. We explore more detailed existence conditions in section 4.1, but a limit cycle will always exist for v_{eq} over the spiking threshold just as in the integrate-and-fire model (large constant current input).

The regular spiking solution for the resonate-and-fire model is defined to start from the reset point at time $t = 0$ and is valid for times up to the period T, when the trajectory crosses threshold.[3]

$$\bar{v}(t) = v_{eq} + r_0 e^{-\lambda t} \cos(t + \theta_0),$$
$$\overline{w}(t) = r_0 e^{-\lambda t} \sin(t + \theta_0),$$

(2.4)

where (r_0, θ_0) are the polar coordinates of the reset point of the limit cycle relative to equilibrium, such that $(v_0, w_0) = (v_{eq} + r_0 \cos \theta_0, r_0 \sin \theta_0)$.

To build a network model of electrically coupled resonate-and-fire oscillators, we introduce diffusive coupling of the voltage variables, i.e., make the coupling linear in the voltage difference between the oscillators. Experiments have shown that electrical coupling current is typically linear and symmetric over a wide range of voltages, particularly for the common channel type connexin-36 [101, 7, 19]. Thus, we include pairwise coupling current terms I_{ij} $(x_i, x_j) = k_{ij}(v_j - v_i)$ in the voltage dynamics, with coupling strengths $k_{ij} = k_{ji}$. However, note

---

[1]Erchova et al. [32] fit subthreshold input-response data from cortical cells to a model of the form (2.2), finding that a subset matched the resonate-and-fire assumptions. Relaxing the assumption of the single time constant in our analysis (allowing distinct λ_v and λ_w) would create an additional parameter dependence for the PRC amplitude and phase only; this adds another dimension of parameter space to the properties of the interaction function, but the functional form of the dynamics, PRC, and interaction function remain the same.
[2]We also note that taking this limit in our phase-reduced model recovers known results for the phase reduction of the leaky integrate-and-fire model [70].
[3]Note that although the spike is not explicit in the resonate-and-fire voltage trajectory, we draw in instantaneous spikes as an indicator of spike timing when plotting v (as in Figure 2.1b), a typical approach for visually representing hybrid neural models.

that exceptions to this form can arise as a result of gap junction channel rectification or asymmetry in cell properties. We briefly discuss the effects of asymmetry in section 6. We also allow parameters of the intrinsic dynamics to vary across cells, introducing heterogeneity that will oppose synchronization. The resulting network model is

$$\frac{dv_i}{dt} = -\lambda_i(v_i - v_{eq}) - \Omega_i w_i + \sum_j I_{ij}(x_i, x_j),$$

$$\frac{dw_i}{dt} = -\lambda_i w_i + \Omega_i v_i.$$

(2.5)

We take the single-oscillator dynamics (2.3) with $W = 1$ as the mean dynamics of the (uncoupled) population, which is the focus of our analysis until we consider network structure in section 5. To complete our definition of the electrically coupled resonate-and-fire model, we need to fill in two details: the reset map in the two-dimensional phase space and the voltage spike itself.

2.4. Details of the reset map.

In multiple dimensions, the reset map need not map all trajectories crossing threshold to a single point as in (2.1). We distinguish a "hard reset," which directly generalizes (2.1) by mapping to a single point x_R [30, 9], from a "soft reset," which allows perturbations to persist over multiple cycles [77, 92]. We consider both hard and soft resets for the resonate-and-fire model. The resonate-and-fire hard reset rule specifies that if the threshold $v_T = 0$ is crossed from below, the state is instantaneously reset to the point $x_R = (v_R, w_R)$.[4]

$$v(t^-) = v_T, \frac{dv}{dt}(t^-) > 0 \Rightarrow x(t^+) = R(x(t^-)) = x_R.$$

(2.6)

Most examples of soft reset models, like the adaptive exponential integrate-and-fire model [10], instead reset voltage to a fixed value while incrementing the adaptation variable. We define the resonate-and-fire soft reset rule as follows, with a fixed increment of the adaptation variable w:

$$v(t^-) = v_T, \frac{dv}{dt}(t^-) > 0 \Rightarrow x(t^+) = R(x(t^-)) = (v_R, w(t^-) + \Delta w).$$

(2.7)

The contrasting modeling choices reflected by these two reset rules can be understood with reference to ion channel gating variables in the Hodgkin–Huxley formalism, which approach a sigmoidal function of voltage at steady state. Gating variables with fast time constants during the spike approach their saturated limits as in the hard reset, whereas slow variables are incremented by an approximately fixed amount that depends on their respective time constants.

---

[4]We note that a reset $v_R = 0$ (i.e., $v_R = v_T$) will leave the cell in "deadlock" on the threshold, as its state following reset still satisfies the reset condition. To resolve this special case, we add the condition that the reset map cannot be applied twice in succession at the same time t.

2.5. Details of voltage spikes.

The definition of an integrate-and-fire model (2.3)–(2.7) typically describes the subthreshold dynamics, threshold crossing, and post-spike reset, but not the suprathreshold portion of the spike itself. Thus, in order to capture the full effects of electrical coupling, with current transfer driven by fluctuations both during and between spikes, we must supplement the model by a description of the effects of the spike. We focus on narrow spikes and with minor assumptions are able to model the spike effects in a parsimonious form that cleanly separates the subthreshold and spike effects in our analysis (section 4.3). Our narrow spike limit is sufficient for most examples of fast sodium action potentials but would need to be extended to account for broader calcium spikes or extremely high frequency spiking.

We assume a cell is insensitive to input during and immediately following the spike, and thus the spike has a characteristic waveform $v_{spike}(t)$ $(0 < t < \tau_{spike})$, regardless of the state of any coupled cells. This assumption reflects observations in experiments and biophysically detailed models of a refractory period where perturbations typically have little to no effect, due to the many ion channels open during an action potential significantly lowering the input resistance of the cell [46].[5]

If we also assume the voltage during the spike is significantly greater than the voltage of any (nonspiking) coupled cells, the integrated current transfer from electrical coupling during the spike is approximated by the constant

$$q_{spike} = \int_0^{\tau_{spike}} k_{12}\big(v_{spike}(t) - v_2(t)\big)dt \approx k_{12}\int_0^{\tau_{spike}} v_{spike}(t)dt \equiv k_{12}M \,.$$

If the time interval of the spike is small relative to the period ($\tau_{spike} \ll T$), the effect of this current on coupled cells is well approximated as an instantaneous transfer of electrical charge, or increment of voltage by $v = q_{spike}$ [69, 89, 70]. We can equivalently represent this effect as a δ-function term in the coupling current for each time a coupled cell spikes (defining S_j as the set of spike times of cell j):

$$I_{ij}\big(x_i, x_j, t\big) = k_{ij}(v_j - v_i) + k_{ij}\Sigma_{t_s \in S_j} M\delta(t - t_s) \,. \tag{2.8}$$

2.6. Notation for general hybrid models.

In order to illustrate the broad applicability of our analysis techniques, we introduce our methods using general notation for an arbitrary hybrid model. The threshold voltage v_T becomes a *threshold manifold* $\mathcal{T}$, with an arbitrary *nonlinear reset map* $R : \mathcal{T} \mapsto \mathcal{R}$ mapping to a corresponding *reset manifold* $\mathcal{R}$. Although a hybrid neuron model can in general consist of any number of dimensions with complex threshold manifolds and reset maps [77], a two-dimensional model is sufficient to illustrate the essential mathematical properties, so we restrict our analysis to models in two dimensions $x = (v, w)$.

---

[5]Note that it would be possible to consider a narrow spike limit of coupling effects without this assumption, leading to slightly different predictions for the contribution of spikes to the electrical coupling effects (section 5.3).

$$\frac{dx}{dt} = \frac{d}{dt}\binom{v}{w} = f(x),\ x(t^-) \in \mathcal{T} \Rightarrow x(t^+) = R(x(t^-)).$$ (2.9)

Note that for the resonate-and-fire model, the threshold manifold and soft reset manifold are both lines of constant voltage $\mathcal{T} = \{(v, w) : v = v_T\}$ and $\mathcal{R} = \{(v, w) : v = v_R\}$, while the reset manifold for hard reset is degenerate, a single point $\mathcal{R} = \{x_R = (v_R, w_R)\}$. We address the possibility of arbitrary orientations and locations of the threshold and reset manifolds in the resonate-and-fire model in section 4.2.

3. Phase reduction theory.

We present a brief introduction in sections 3.1–3.3, followed by an explanation of the aspects of the derivation unique to hybrid models in section 3.4. Readers already familiar with the theory of weakly coupled oscillators can skip directly to section 3.4.

3.1. Phase mapping for weakly coupled oscillators.

The theory of weakly coupled oscillators is a method of model reduction with the goal of creating simpler models for the dynamics of interacting limit-cycle oscillators. The state of each oscillator is mapped to a single variable: the phase (or timing) of oscillations. This process is referred to as "phase reduction" and the result as a "phase model." The oscillators' intrinsic dynamics and the coupling between oscillators together determine the *interaction function*, which captures the modulation of instantaneous frequency caused by coupling. This scalar function defines the coupling between the phase oscillators and thus determines the dynamics of the coupled system (together with any heterogeneity of intrinsic frequencies). Dynamical properties such as the stability of phase-locked states can be directly assessed from features of the interaction function, as we will show in section 5. Although a formal derivation assumes weak coupling and weak heterogeneity, predictions from the phase model often remain valid even at moderate levels of coupling. Here we first provide a brief derivation of the phase model for a continuous coupled oscillator system. We then explain the specific challenges presented by hybrid systems and our approach to overcoming these challenges.

We note that the phase reduction approach can also be augmented by considering a second coordinate to capture motion transverse to the limit cycle, following a construction closely resembling that which we present here for phase [5, 107, 110, 98, 109], and which has recently been extended to nonsmooth dynamics [108]. In the case of the simple models we study here such a reduction would do little to simplify the dynamics, but in other cases a second coordinate can allow reduction under fewer conditions and may generate more realistic predictions.

The dynamics of a general system of coupled oscillators are described by

$$\frac{dx_i}{dt} = f(x_i) + g_i(x_i) + \sum_j k_{ij} I_c(x_i, x_j).$$ (3.1)

The state space of each individual oscillator is $x_i \in \mathbb{R}^n$, where n is the dimension of the oscillator model. The intrinsic dynamics of each oscillator are defined by $f+g_i$, where f gives an average of the intrinsic dynamics across all oscillators, and g_i captures the heterogeneity of the oscillators. We assume the average dynamics to have an asymptotically stable T-periodic limit cycle $\bar{x}(t)$ defined by

$$\frac{d\bar{x}}{dt} = f(\bar{x}), \ \bar{x}(t+T) = \bar{x}(t).$$ (3.2)

We have also restricted the pairwise coupling $I_{ij}(x_i, x_j)$ to a common functional form defined by the coupling function I_c, which is weighted by connection strengths k_{ij} and summed over all pairs to give the total coupling. The phase reduction requires the assumption of weak coupling and weak heterogeneity, meaning that the heterogeneity g_i and the total coupling term must both be small compared to the average intrinsic dynamics f.

To reduce the model for this coupled system, we define a *phase mapping* $\Theta : \mathbb{R}^n \mapsto S^1$, from the state x to a scalar phase variable θ, that uniquely identifies points on the limit cycle. The dynamics of the coupled system are translated through this mapping to define the phase model,

$$\frac{d\theta_i}{dt} = \omega_i + \sum_j k_{ij} H\big(\theta_j - \theta_i\big).$$

The dynamics of this reduced system depend only on the interaction function H and the heterogeneity of frequencies ω_i. Below, we show how these are derived from the coupling I_c and heterogeneity g_i of the full model.

We first define the phase map for points on the limit cycle, giving a periodic "time" coordinate,

$$\theta = \Theta(\bar{x}(t)) \equiv t.$$ (3.3)

Phase is unique modulo T, with $\theta = 0$ determined by our choice of initial condition $\bar{x}(0)$ for the reference limit cycle. (Note that phase is sometimes rescaled to a period of 1 or 2π, but we choose to keep the natural units of time.)

The phase map can then be extended beyond the limit cycle to give the "asymptotic phase" of all points in the basin of attraction. Trajectories that eventually converge are assigned the same phase, i.e.,

$$\Theta(x(t)) = \Theta(\bar{x}(\theta)) = \theta \text{ iff } \lim_{t' \to \infty} \big[x(t+t') - \bar{x}(\theta+t')\big] = 0.$$ (3.4)

3.2. Phase response curve and the adjoint method.

The full phase mapping is difficult to find analytically in all but the simplest contexts. Fortunately, the weak coupling assumption allows the phase reduction to proceed with a

linear approximation of the mapping about the limit cycle $\bar{x}(t)$, which is much easier to compute. For a trajectory close to the limit cycle, phase can be approximated as linearly dependent on the deviation away from the limit cycle, $x(t)$.

$$\Theta(x(t)) = \Theta(\bar{x}(t) + \Delta x(t)) \approx \Theta(\bar{x}(t)) + \nabla\Theta(\bar{x}(t))^T \Delta x(t). \tag{3.5}$$

The *infinitesimal* phase response curve (iPRC or PRC, also called the "phase sensitivity function") Z is defined as the proportional shift in phase caused by infinitesimal perturbations to the limit cycle,

$$Z(\theta) = \nabla\Theta(\bar{x}(\theta)). \tag{3.6}$$

Note that the PRC is naturally defined as a vector-valued function, giving the effect of perturbations to each state variable. In the context of neural synchrony, however, the voltage component is usually most important, because perturbations tend to be currents and thus directly affect only the current balance equation for the dynamics of voltage.

A direct method to approximate the PRC either experimentally or computationally is simply to measure phase shifts caused by many small but finite perturbations. We instead follow the "adjoint method," which derives and solves a differential equation for the PRC tied to the limit-cycle dynamics. Below we provide a brief exposition that captures the essence of this method and its proof.

From the definition of asymptotic phase (3.4), the phase difference between the limit cycle $\bar{x}(t)$ and a nearby trajectory $x(t)$ must be constant in time. That is, the separation $\Delta x(t) = x(t) - \bar{x}(t)$ must satisfy

$$c = \Theta(\bar{x}(t) + \Delta x(t)) - \Theta(\bar{x}(t)) \approx Z(t)^T \Delta x(t),$$
$$0 \approx \frac{d}{dt}\left(Z(t)^T \Delta x(t)\right). \tag{3.7}$$

To first order, the deviation from the limit cycle $x(t)$ evolves according to the Jacobian matrix of derivatives of the system dynamics, Df, evaluated on the limit cycle given by (3.2).

$$\frac{d}{dt}\Delta x(t) \approx Df(\bar{x}(t))\Delta x(t).$$

Substituting this expression into (3.7), we obtain

$$\left(\frac{dZ(t)^T}{dt} + Z(t)^T Df(\bar{x}(t))\right)\Delta x(t) = 0.$$

Because this holds for any x, Z must satisfy the following T-periodic linear differential equation known as the adjoint equation, defined by the adjoint of the linearized limit-cycle dynamics,

$$\frac{dZ(t)}{dt} + Df(\bar{x}(t))^T Z(t) = 0. \tag{3.8}$$

The PRC is the unique periodic solution of (3.8), given a normalization constraint that follows from our definition of phase on the limit cycle (3.3).

$$1 = \frac{d}{dt}\Theta(\bar{x}(t)) = Z(t)^T f(\bar{x}(t)), \ t \in [0, T]. \tag{3.9}$$

Note that if this constraint is satisfied at any single time, (3.8) ensures it will remain satisfied for all time.

3.3. The phase model and interaction function.

Using the PRC result derived via the adjoint method, we can complete the derivation of the phase reduction of the coupled oscillator system (3.1). The effect of any weak time-dependent perturbation on the phase of an oscillator, including the effect of coupling, is governed by the PRC. Specifically, if the dynamics of the limit cycle are weakly perturbed according to $\frac{dx}{dt} = f(x) + \epsilon p(t)$ (for $\epsilon \ll 1$), the perturbed phase $\theta = \Theta(x(t))$ satisfies

$$\frac{d\theta}{dt} = \nabla\Theta^T \frac{dx}{dt} \approx 1 + \epsilon Z(t)^T p(t).$$

Since the perturbation is weak, its effects occur on a slow timescale, $\mathcal{O}(\epsilon)$, which can be separated from the faster dynamics of unperturbed phase, $\frac{d\theta}{dt} = 1$. If the perturbation is also periodic with the intrinsic period T, this separation allows us to eliminate the explicit time-dependence $p(t)$ by averaging the slow effect of coupling over a full period of the fast phase dynamics.

Because the perturbations that define the coupled population model (3.1) are close to periodic, their effects can be approximated by the method of averaging.[6] The heterogeneity and coupling perturbations to an oscillator are functions of its own trajectory x_i and those of the other oscillators x_j. Each trajectory is approximated by the T-periodic average limit cycle, $x_i \approx \bar{x}(\theta_i)$ (where $\theta_i = \Theta(x_i)$); therefore, we can approximate these perturbations (to order ϵ) as periodic functions of phase, $g_i(x_i) \approx \tilde{g}_i(\theta_i) \equiv g_i(\bar{x}(\theta_i))$ and likewise for $\tilde{I}_c$.

$$\frac{dx_i}{dt} \approx f(x_i) + \overbrace{\left[\tilde{g}_i(\theta_i) + \sum_j k_{ij}\tilde{I}_c(\theta_i, \theta_j)\right]}^{\epsilon p(t)}.$$

The final result of the phase reduction is the phase model, i.e.,

---

[6]A more detailed explanation of the phase reduction can be derived from singular perturbation theory or averaging theory [40, 96].

$$\frac{d\theta_i}{dt} = \omega_i + \sum_j k_{ij} H(\theta_j - \theta_i), \tag{3.10}$$

where

$$\omega_i = 1 + \frac{1}{T} \int_0^T Z(t)^T \tilde{g}_i(t) dt, \tag{3.11}$$

$$H(\theta_j - \theta_i) = \frac{1}{T} \int_0^T Z(t)^T \tilde{I}_c(t, t + \theta_j - \theta_i) dt. \tag{3.12}$$

The frequency term ω_i arises from the intrinsic heterogeneity in cellular properties, and the interaction function H from the coupling. We note that the form of H as a function of phase differences, $\phi_{j-i} = \theta_j - \theta_i$, arises from the application of averaging.

3.4. PRC for hybrid models.

For hybrid models, the PRC as well as the trajectory may be discontinuous at the threshold crossing. Without the periodicity constraint acting as a boundary condition, the adjoint equation (3.8) with normalization (3.9) no longer has a unique solution, and a naive application of the adjoint method fails to find the PRC. Intuitively, the resolution is to find the appropriate "reset" map or boundary condition for the PRC. Shirasaka, Kurebayashi, and Nakao [98] present a boundary condition linked to the *saltation matrix*, a correction to the linearized dynamics of a hybrid system to account for discontinuity across a boundary [8, 68, 3]. They prove that the solution to the adjoint problem with their boundary condition gives the PRC for the asymptotic phase of hybrid systems. Related results have been independently presented by Park et al. [87] for nonsmooth systems with discontinuous boundaries but no reset map and by Ladenbauer et al. [64] for a specific hybrid neuron model. We present a brief heuristic derivation for an equivalent adjoint boundary condition and show that the condition has an intuitive form tied to the geometry of the threshold. We assume the existence of a phase mapping in a neighborhood about the limit cycle which is differentiable everywhere except in the transverse direction across the threshold and reset manifolds. This is equivalent to assuming the existence of a well-defined PRC. For additional discussion of this assumption, see [98].

Consider a limit cycle trajectory $\bar{x}(t)$, reaching the threshold manifold at $\bar{x}(T) = x_T = (v_T, w_T)$, as shown in Figure 3.1. The phase on this trajectory cannot change across the instantaneous reset. That is, since $\Theta(\bar{x}(t))$ must be continuous in t,

$$\Theta(x_T) = \lim_{t \to T^-} \Theta(\bar{x}(t)) = \lim_{t \to T^+} \Theta(\bar{x}(t)) = \Theta(R(x_T)), \tag{3.13}$$

where the right limit of the reset discontinuity is given by the reset point $R(x_T)$. We introduce a unit tangent vector u along the threshold manifold $\mathcal{T}$ at x_T (Figure 3.1). Given

the assumed differentiability of the phase mapping, we can apply a directional derivative along this tangent vector (D_u) to both sides of (3.13).

$$
\begin{aligned}
D_u \Theta(x_T) &= D_u \Theta(R(x_T)), \\
\nabla \Theta(x_T)^T u &= \nabla \Theta(R(x_T))^T D_u R(x_T), \\
Z_u(T^-) &= (D_u R(x_T))^T Z(0^+).
\end{aligned}
\tag{3.14}
$$

This equation gives a boundary condition for the PRC, replacing the standard assumption of periodicity. As long as the limit cycle is not tangent to the boundary (the transverse flow condition of [87]), (3.14) is independent of the normalization condition (3.9), and together they determine the unique solution to the adjoint problem for the discontinuous limit cycle of the hybrid model. Note that the derivative of the reset map is only defined in directions tangent to the threshold, so there is no corresponding constraint on the perpendicular component of the PRC. In N dimensions the threshold manifold is $(N-1)$-dimensional, so rather than a single vector u, we enforce (3.14) for each of $N-1$ vectors u_i spanning the tangent space.[7]

This boundary condition expresses an intuitive fact about perturbations to the limit cycle: the phase difference between the limit cycle and a trajectory perturbed along the threshold (given by $Z_u(T^-)$) must be the same as the difference after both trajectories are reset. The difference after reset is expressed by the PRC at the reset point, $Z(0^+)$, with the perturbation transformed by the reset map to a distinct perturbation along the reset manifold, approximated by $D_u R$ (Figure 3.1).

4. Phase reduction of the resonate-and-fire model.

4.1. Existence and stability of spiking limit cycles.

Before applying the theory of phase reduction to any model, we must ensure the system exhibits a stable limit cycle. We begin our analysis of the resonate-and-fire model by finding the existence and stability conditions for spiking limit cycles. These conditions define boundaries of the stable limit cycle regime in parameter space, i.e., bifurcations of the resonate-and-fire model.

Hard reset.—We first discuss the existence conditions of the spiking limit cycle with hard reset, (2.6). The spiking limit cycle exists whenever a trajectory starting from the reset point crosses the threshold. The limit cycle is lost in a "grazing bifurcation" when the trajectory becomes tangent to and then fails to cross the firing threshold. Beyond this bifurcation, trajectories show decaying subthreshold oscillations, approaching rest at the equilibrium voltage. The hard reset map ensures that the spiking limit cycle is always stable, as the reset erases all effects of small perturbations to the cycle by projecting to the single reset point.

We can visualize the spiking regime boundaries in a two-dimensional parameter space that captures the most important dimensions of variability of the model dynamics. We choose a

---

[7]By extending the reset map to a neighborhood of the boundary, Shirasaka, Kurebayashi, and Nakao [98] instead present N conditions; the Nth condition missing from our analysis is redundant if the normalization condition (3.9) is enforced at all times (see section A.2).

small decay parameter $\lambda = 0.1$ to give slowly decaying subthreshold oscillations. The dynamics then depend on the reset parameters v_R and w_R as well as the equilibrium v_{eq}, but because the model is invariant to uniform rescaling of the (v, w) phase space, we can rescale to $|v_R| = 1$ without loss of generality. Therefore, in Figure 4.1 we explore two distinct two-dimensional (v_{eq}, w_R) parameter spaces for positive and negative reset voltage, fixed at $v_R = \pm 1$ (see Figure 2.1a). In both the negative and positive reset regimes, a single grazing bifurcation occurs for low equilibrium voltage v_{eq} (negative tonic input current), below which the model is quiescent (at rest). In the positive reset regime, a second grazing bifurcation occurs for high v_{eq}, when the voltage fails to dip below threshold, corresponding to depolarization block. The bifurcations shown in Figure 4.1 curve away from the origin because any increase in the magnitude of the adaptation variable reset w_R increases the radius of the orbit, moving the system away from the bifurcation. We can express the tangency condition for the grazing bifurcation in terms of the orientation of the trajectory when crossing threshold, $\theta_H = \tan^{-1}\left(\frac{dw/dt(T)}{dv/dt(T)}\right)$. At the bifurcation, this orientation matches that of the threshold,

$$\theta_H = \theta_0 + T + \frac{\pi}{2} + \tan^{-1}\lambda = \pm\frac{\pi}{2}. \tag{4.1}$$

Soft reset.—Although the subthreshold dynamics always lead to decay of perturbations, the soft reset map can in some cases amplify perturbations, making the limit cycle unstable. In addition to the grazing bifurcation boundaries, the stable spiking regime can also be lost in a saddle-node bifurcation of limit cycles, where the stable and unstable cycles collide and annihilate. In addition, the dynamics with soft reset allow for limit cycles with multiple spikes, and we will show that the spiking limit cycle can also lose stability in a period-doubling bifurcation.

To determine existence and stability conditions for the soft reset limit cycles, we reduce the dynamics to a Poincaré return map on the reset manifold (also referred to as an adaptation map [104]). This map takes a value of the adaptation variable at the kth reset, w_k, to the value at the following reset, $w_{k+1} = P(w_k)$. A limit cycle corresponds to a fixed point of the map, $\overline{w} = P(\overline{w})$, and the cycle is asymptotically stable if the fixed point satisfies $\left|\frac{dP}{dw}(\overline{w})\right| < 1$.

The derivative of the return map characterizes the degree of attraction to the limit cycle and is therefore also tied to the validity of the asymptotic approximation of the phase reduction. We begin by deriving the return map for a general reset map from the threshold (v_T, w) to $R(w) = (v_R, R_w(w))$. We then evaluate the fixed points and their stability for the soft reset map.

We define the flow of the resonate-and-fire system $F(w_k, t) = x(t) = (v(t), w(t))^T$, where the trajectory $x(t)$ satisfies the subthreshold dynamics from (2.3) starting from an initial condition $x(0) = (v_R, w_k)^T$ on the reset manifold. The flow evaluates to

$$F(w_k, t) = \begin{pmatrix} F_v \\ F_w \end{pmatrix} = e^{-\lambda t}\begin{pmatrix} \cos t & -\sin t \\ \sin t & \cos t \end{pmatrix}\begin{pmatrix} v_R \\ w_k \end{pmatrix}. \tag{4.2}$$

We then define the spike time map $\tau(w_k)$, giving the time it takes such a trajectory to reach the threshold,

$$\tau(w_k) = \min\{t \ : \ F_v(w_k, t) = v_T\}. \tag{4.3}$$

A trajectory starting at w_k crosses threshold at the point $F(w_k, \tau(w_k))$ and is reset to $R(F_w(w_k, \tau(w_k)))$. The w-component of this reset point, R_w, gives the desired return map,

$$w_{k+1} = P(w_k) = R_w(F_w(w_k, \tau(w_k))). \tag{4.4}$$

A fixed point $\bar{w} = w_0$ of the return map corresponds to a limit cycle with period $T = \tau(w_0)$. The stability of a limit cycle with soft reset is assessed by evaluating the derivative of the return map for the soft reset rule $R_W(w) = w + \ \ w$ (2.7).

$$\begin{aligned}
\frac{dP}{dw}(w_0) &= \frac{dR_w}{dw}(w_T)\left(\frac{\partial F_w}{\partial w}(w_0, T) + \frac{\partial F_w}{\partial t}(w_0, T)\frac{\partial \tau}{\partial w}(w_0)\right) \\
&= \left(\frac{\partial F_w}{\partial w}(w_0, T) - \frac{dw}{dt}(T)\frac{\frac{\partial F_v}{\partial w}(w_0, T)}{\frac{dv}{dt}(T)}\right) \\
&= e^{-\lambda T}(\cos T + \tan\theta_H \sin T),
\end{aligned}$$

where we recall the trajectory's orientation at threshold $\theta_H = \theta_0 + T + \frac{\pi}{2} + \tan^{-1}\lambda$. For the soft reset rule then, the limit cycle can be stable or unstable depending on the decay λ and the geometry of the threshold and reset manifolds. Loss of stability occurs when

$$\pm 1 = \frac{dP}{dw}(w_0) = e^{-\lambda T}(\cos T + \tan\theta_H \sin T),$$

which implies that bifurcations occur in the full resonate-and-fire model when

$$\tan\theta_H = \frac{\pm e^{\lambda T} - \cos T}{\sin T}. \tag{4.5}$$

The negative slope instability (at $\frac{dP}{dw} = -1$) corresponds to a subcritical period-doubling bifurcation (proof not shown), where an unstable period-two limit cycle collides with a stable period-one limit cycle. The positive slope instability corresponds to a saddle-node bifurcation of limit cycles, with a stable cycle coalescing either with a finite unstable cycle or at infinity (return map slope approaching unity as $w_0 \to -\infty$ for finite parameter values).

In Figure 4.2, we plot the stability of the limit cycle $\frac{dP}{dw}(w_0)$ and the grazing bifurcations for soft reset together in (v_{eq}, w_0) parameter space. Since w_0 corresponds to the parameter w_R for hard reset, the grazing bifurcations (solid lines in Figure 4.2) are identical to the hard reset grazing bifurcations in (v_{eq}, w_R) coordinates from Figure 4.1. The loss of stability bifurcations and the grazing bifurcations form the two boundaries of a narrow unstable limit cycle regime. These bifurcations are both related to threshold crossing and necessarily lie

close together. Perturbations are amplified by the reset map, causing instability, because of a mismatch between the angles of incidence with the threshold and reset manifolds, which increases as the trajectory approaches tangency to the threshold (the grazing bifurcation condition). We note that, near the saddle-node bifurcations, the return map can have two fixed points, representing stable and unstable cycles. The representation in Figure 4.2 unfolds the bifurcation so that a single point in the parameter space (v_{eq}, w) corresponds to two points in (v_{eq}, w_0) space, stable and unstable cycles on opposite sides of the dashed bifurcation line.

4.2. Resonate-and-fire PRC.

The first step in proceeding with the phase reduction of the resonate-and-fire model is to evaluate its phase response curve (PRC), expressing the effect of perturbations to the limit cycle as a proportional phase shift (section 3.2). In general, the PRC can be evaluated either by direct calculation or by the adjoint method. Although directly calculating the effect of perturbations typically must be carried out computationally, the resonate-and-fire model with hard reset allows the PRC to be calculated directly from an analytical expression for phase [80]. Since all points on the threshold are mapped onto the single point x_R, the threshold can serve as a reference point to define the phase map for all trajectories. However, we choose instead to derive the PRC from the adjoint equation with a general reset rule, following the theory described in section 3.4. This approach allows us to see the hard reset as a special case and to capture the geometric intuition in the relationship between the dynamics, the adjoint equation, and the reset rule.

We proceed by first evaluating the adjoint equation (3.8) for the subthreshold dynamics. In general, the adjoint equation evaluates the dynamics linearized about the limit cycle. Since the resonate-and-fire dynamics (2.3) are linear, the adjoint equation is simply defined by the negative transpose of the time-independent linear operator,

$$\frac{dZ}{dt} = -Df(\bar{x})^T Z = \begin{pmatrix} \lambda & -1 \\ 1 & \lambda \end{pmatrix} Z . \tag{4.6}$$

The PRC solution exhibits exponentially growing oscillations:

$$Z_v(t) = \frac{A}{r_0} e^{\lambda t} \cos(t - T + \alpha),$$
$$Z_w(t) = \frac{A}{r_0} e^{\lambda t} \sin(t - T + \alpha) . \tag{4.7}$$

The PRC is defined as written for times $0 < t < T$ and extends periodically to all t modulo T, with a discontinuity at $t = 0$ (due to the discontinuous reset map skipping over dynamics during the spike). The amplitude $A = \dfrac{1}{\sqrt{1 + \lambda^2} \cos(\theta_H - \alpha)}$ is determined by the normalization condition,

$$Z(t) \cdot \frac{dx}{dt}(t) = 1, \ t \in (0, T) . \tag{4.8}$$

Based on the reset map, the boundary condition for the adjoint equation (3.14) links the left and right limits of the discontinuity, determining the phase shift a. Examples of the v-component PRC for both positive and negative v_R are shown in Figure 4.3.

The general form for the boundary condition from (3.14) simplifies given our assumption that the threshold and reset manifolds are in the w-direction (constant v), with reset map R_w (w),

$$Z_w(T^-) = \frac{dR_w}{dw}(w_T)Z_w(0^+).$$

(4.9)

For the hard reset (2.6), mapping to a constant reset point, the derivative of the reset map is zero. Thus (4.9) reduces to the terminal condition $Z_w(T^-) = 0$, corresponding to a phase $a = 0$. This result is equivalent to the geometric constraint that the PRC must be perpendicular to the threshold, or oriented in the v-direction at time T. That is, perturbations along the threshold have no effect after the reset.

For the soft reset rule (2.7), an increment of w, the boundary condition (4.9) mandates continuity of the w-component of the PRC, $Z_w(T^-) = Z_w(0^+)$. Intuitively, this tells us that a perturbation to w immediately before the spike has the same effect as a perturbation after the spike; i.e., perturbations tangent to the threshold are unchanged by the soft reset map. This continuity boundary condition leads to a phase shift of Z_v,

$$\alpha = \arctan\left(\frac{\sin T}{\cos T - e^{\lambda T}}\right).$$

(4.10)

This phase shift is typically small for positive v_R but can grow more significant in parts of the negative reset regime. (See an example in Figure 4.3 and the full calculation in section A.3.)

We note that in the more general case of a nonlinear reset map, the result depends on $\frac{dR_w}{dw}$, for which the hard and soft resets are the special cases $\frac{dR_w}{dw} = 0$ and 1, respectively. A nonlinear reset map with derivative close to either extreme would lead to small corrections to the corresponding a value. Similarly, small variations in the orientation of the threshold or reset manifold lead to minor adjustments to (4.9) and to the resulting phase shift a.

We also note that the amplitude A has a singularity when

$$\cos(\theta_H - \alpha) = 0.$$

(4.11)

This singularity is associated with the high sensitivity to perturbations near bifurcations of the limit cycle. For the hard reset $a = 0$, $\theta_H = \pm\frac{\pi}{2}$ is the grazing bifurcation condition (4.1).

For the soft reset, the singularity occurs when $\tan\theta_H = -\cot\alpha = \frac{e^{\lambda T} - \cos T}{\sin T}$, which is condition (4.5) for the saddle-node bifurcation of the limit cycle (positive slope instability of the return map). Interestingly, the negative slope loss of stability (period-doubling

bifurcation) is not reflected in the PRC. It seems that in the positive slope instability, phase shifts continue to accumulate progressively on each cycle, whereas in the negative slope case, positive and negative phase shifts alternate as they grow, leading the PRC to reflect an averaged finite phase shift that fails to capture the loss of stability.

4.3. Phase model of electrically coupled resonate-and-fire neurons.

We now proceed to construct the interaction function and phase model for electrically coupled resonate-and-fire neurons. In the weak coupling regime, this reduced model with a single phase variable for the state of each oscillator captures the full synchronization properties of the resonate-and-fire network (2.5). We explore how the phase model changes as we vary the equilibrium voltage and reset parameters, representing different cell types and classes of firing dynamics.

The interaction function H and heterogeneity ω of the phase model are calculated according to (3.10), from the electrical coupling and heterogeneity of frequencies in the full model along with the PRC from (4.7). The heterogeneity of frequencies in the phase model represents a combination of all parameter heterogeneity in the resonate-and-fire network model, as described by the integral (3.11). We assume a fixed level of frequency heterogeneity (relative to the mean $\omega = 1$) and thus focus on how parameter changes affect the interaction function H.

The interaction function H defines the nonlinear coupling between cells in the phase model. It can be expressed as a convolution integral of the coupling current and the PRC, according to (3.12). In the case of electrical coupling, the coupling function $I_c = v(t + \phi) - v(t) + M\delta(t + \phi)$ (cf. (2.8)) contains terms for the subthreshold voltage difference and the spike of the coupled cell. The resulting interaction function, depicted in Figure 4.4, is

$$H(\phi) = \frac{1}{T} \int_0^T Z_v(t)[v(t + \phi) - v(t) + M\delta(t + \phi)]dt, \phi \in [0, T]. \tag{4.12}$$

Since the interaction function convolves the PRC and the coupling function, with a linear dependence on both, we can additively separate the corresponding subthreshold and spiking components, $H = H_{sub} + H_{spike}$:

$$H_{sub}(\phi) = \frac{1}{T} \int_0^T Z_v(t)[v(t + \phi) - v(t)]dt,$$

$$H_{spike}(\phi) = \frac{M}{T} \int_0^T Z_v(t)\delta(t + \phi)dt.$$

The spike (δ-function) component of the coupling function determines the *spike interaction function* H_{spike}, representing the effect of this voltage transient through the electrical coupling. This is essentially a pulse-coupling interaction, as used in simple models of excitatory chemical synapses [78, 63, 79]. In the narrow spike limit that we study, the effect is entirely determined by the PRC and the magnitude of the spike, and the spike interaction function can be discontinuous at the origin, as shown in Figure 4.4. We return to the effects of this interaction in section 5.3.

The *subthreshold interaction function H_{sub}* captures the effect of subthreshold fluctuations of the limit cycle. Analysis of this component allows us to determine how the resonant properties of the model contribute to synchronization. Each parameter of the model affects synchronization both through its effect on the limit cycle and on the PRC, making the combined effect (encoded by H_{sub}) potentially complex. The only general constraints on the subthreshold interaction function are that it must be continuous and pass through the origin; $H_{sub}(0) = 0$ because the gap junction coupling is diffusive, proportional to the difference of voltages.

The interaction function integral for the subthreshold component results in a complex expression, in part because the integral must be split due to the discontinuity of the orbit (full calculation in section A.4). To simplify the analysis, we split the subthreshold interaction function into three terms with distinct parameter dependence:

$$H_{sub}(\phi) = A_{C1}C1(\phi) + A_{C2}C2(\phi) + A_S S(\phi),$$
$$C1(\phi) = 1 - \frac{e^{-\lambda\phi}}{T}\left[e^{\lambda T}\phi\cos(T - \phi) + (T - \phi)\cos\phi\right],$$
$$C2(\phi) = \frac{e^{-\lambda\phi}}{T}\left[e^{\lambda T}\sin\phi + \sin(T - \phi)\right] - \frac{\sin T}{T},$$
$$S(\phi) = \frac{e^{-\lambda\phi}}{T}\left[-e^{\lambda T}\phi\sin(T - \phi) + (T - \phi)\sin\phi\right].$$

(4.13)

$$A_{C1} = -\frac{A}{2}\cos(\theta_T - \alpha), \quad A_{C2} = \frac{A}{2}\cos(\theta_0 + \alpha), \quad A_S = -\frac{A}{2}\sin(\theta_T - \alpha),$$

(4.14)

where $\theta_T = \theta_0 + T$ is the angular coordinate of the trajectory at threshold. We note that the *S*-function closely resembles sine, while the two *C*-functions resemble a vertically shifted cosine, as shown in the example in Figure 4.5. This approximate odd and even symmetry about the origin means they contribute in distinct ways to synchronization of simple networks. In the following sections, we consider these effects by studying networks of two and three cells.

5. Synchronization of two electrically coupled resonate-and-fire neurons.

Our primary goal with the phase reduction of the resonate-and-fire model is to provide insight into the synchronization of networks of electrically coupled resonant neurons. Even after phase reduction, the analysis of large systems with realistic network architecture is hindered by the nonlinear phase coupling and number of degrees of freedom, and in general must be carried out numerically. Therefore, we focus on minimal networks of two or three cells and save the analysis of large-scale networks for future work. In this idealized context, we can explain how the cellular properties of the resonate-and-fire oscillators determine network synchrony through the distinct components of the interaction function (in terms of slopes, amplitudes, and discontinuities). Although large networks cannot be completely understood by their two-and three-cell subnetworks, in many cases the intuition built on these minimal networks holds [2].

5.1. General considerations.

We begin by examining the synchronization of a symmetrically coupled pair of oscillators, the simplest and most commonly analyzed network [36, 62, 69, 74]. The assumption of symmetry implies that the equation governing the phase difference between the oscillators (5.2) isolates a component of the interaction function with odd symmetry, simplifying the analysis. Experiments have shown that electrical coupling is often close to symmetric, especially when between the same cell type and formed by the common symmetric channel type connexin-36 [7]. Nonetheless, asymmetry can and does arise, either from rectification (favoring current flow in one direction) in the gap junction channels that make up the electrical synapse, or from asymmetries in size or gap junction location. We will address the effects of asymmetry briefly in section 6.

The phase model (3.10) for a pair of symmetrically coupled oscillators ($k_{12} = k_{21} = K$) is given by

$$\dot{\theta}_i = \omega_i + KH(\theta_j - \theta_i).$$ (5.1)

Expressed in terms of the phase difference $\phi_{i-j} = \theta_i - \theta_j$ and frequency difference $\Delta\omega_{1-2}$, we can rewrite (5.1) in terms of the odd component of the H function, $H_{odd}(\phi) = \frac{1}{2}(H(\phi) - H(-\phi)) = H(\phi) - H_{even}(\phi)$, as follows:

$$\dot{\phi}_{1-2} = \Delta\omega_{1-2} - 2KH_{odd}(\phi_{1-2}).$$ (5.2)

(Some analyses refer to the G-function, $G(\phi) = -2H_{odd}(\phi)$ [96]). Fixed points of (5.2) correspond to phase-locked states of the coupled pair, the existence and stability of which are determined by properties of H_{odd}, as depicted in Figure 5.1a and described below.

For identical oscillators ($\Delta\omega_{1-2} = 0$), the odd symmetry of (5.2) implies a pair of fixed points at $\phi_{1-2} = 0$ and $\phi_{1-2} = T/2$ for synchronous and antiphase states, respectively. If H_{odd} has only a single local maximum, which is typical for the electrically coupled resonate-and-fire model, only one of these two fixed points is stable and no additional fixed points exist. The synchronous state is stable and the antiphase state unstable when the slope $H'_{odd}(0)$ is positive, and the reverse holds for negative slope. (For simplicity, we shorten references to the slope evaluated at the origin to "slope.") For hybrid models, the slope of the full interaction function $H'(0)$ may be undefined, with different right and left limits, but the odd symmetry forces $H'_{odd}(0)$ to always be well defined.

We note that in larger networks a similar dependence on the slope exists. Typically, a strong positive slope leads to global synchrony, while a negative slope leads to global incoherence [2]. Nonetheless, in some cases global features of the interaction function $H(\phi)$ can have significant effects of synchronization; the even component effects we discuss in section 6 are one example.

As the frequency heterogeneity of the pair increases, the pair of fixed points shifts progressively in the relative phase of the oscillators. We refer to these states as near-synchronous and near-antiphase. For small frequency heterogeneity $\Delta\omega_{1-2} > 0$, the phase

difference in the near-synchronous state is approximately inversely proportional to the slope, $\phi_{1-2} \approx \frac{\Delta\omega_{1-2}}{2KH'_{odd}(0)}$. Note that this phase difference is in units of time, while to compare phase-locked states across oscillators with different periods we should evaluate phase in radians. To account for this we rescale both the phase and the slope H'_{odd},

$$\hat{\phi}_{1-2} = \phi_{1-2}\frac{2\pi}{T} \approx \frac{\Delta\omega_{1-2}}{2K\widehat{H}'_{odd}(0)}, \text{ where } \widehat{H}'_{odd}(0) \equiv \frac{T}{2\pi}H'_{odd}(0).$$

(Note that here we use prime to denote the slope of both functions, so H' is a time derivative and $\widehat{H}'$ is a phase derivative.)

For larger heterogeneity, the phase difference continues to increase until ω_{1-2} is greater than the amplitude of $2KH_{odd}$ (red level in Figure 5.1a). At this point the fixed points of (5.2) are lost in a saddle-node bifurcation, and the phase-locked state transitions to "phase walk-through," with the phases of the cells slipping past each other (red curve in Figure 5.1b right).

We can thus quantify the robustness of synchrony to heterogeneity in two ways: for fixed coupling K, the slope $\widehat{H}'_{odd}(0)$ gives the strength of synchrony for small heterogeneity, while the amplitude of H_{odd} gives the critical heterogeneity at which the near-synchronous state is lost. Due to the noise and heterogeneity present in biological systems, we consider robustness to be an important criterion for synchronization in addition to the stability of the synchronous state for identical oscillators. Below, we consider the robustness and stability of near-synchronous phase-locking in more detail for the subthreshold and spiking components of the interaction function for electrically coupled resonate-and-fire neurons.

5.2. Subthreshold contribution.

For the analysis of synchrony in the electrically coupled resonate-and-fire model, we begin by evaluating the contribution to the odd component of the subthreshold interaction function H_{sub} and return to the spiking component in section 5.3. For the subthreshold interaction function the odd component is typically dominated by the first Fourier component $\widehat{H}_{odd}(\hat{\phi}) \propto \sin(\hat{\phi})$, so its slope and amplitude, our two measures of robustness, are roughly proportional (see section A.6). We first identify the condition for stable synchrony (positive slope) and show that the subthreshold contribution is virtually always synchronizing, with negative slope only possible along the spiking regime boundary. We then explore the robustness of synchrony as measured by the magnitude of the positive slope, identifying a dependence on the shape of the voltage trajectory through the reset voltage v_R.

We split the calculation of the slope of H_{sub} into components, following the decomposition (4.13) of component functions with approximate symmetry (see Figure 4.5). We consider the limit of small decay ($\lambda \ll 1$) by expanding to first order in the decay parameter (see calculation in section A.5).

$$2\pi\widehat{C}1'_{odd}(0) = \lambda T - \cos T \sinh(\lambda T) \approx \lambda T(1 - \cos T) > 0,$$
$$2\pi\widehat{C}2'_{odd}(0) = \sinh(\lambda T) - \lambda \sin T \approx \lambda(T - \sin T) > 0, \tag{5.3}$$
$$2\pi\widehat{S}'_{odd}(0) = T - \sin T \cosh(\lambda T) \approx T - \sin T > 0.$$

The $O(1)$ in λ contribution to $\widehat{H}'_{odd}(0)$ from S is the primary subthreshold factor determining the strength and stability of synchrony (as shown in Figure 4.5). The sign of this slope is determined by A_S, the coefficient of the S component. Specifically, the condition for stable synchrony is approximated to order λ by

$$A_S = -\frac{A}{2}\sin(\theta_T - \alpha) = \frac{A}{2}\cos\left(\theta_T + \frac{\pi}{2} - \alpha\right) > 0.$$

Note that the boundary of this stable region differs only to order λ from the PRC singularity condition (4.11),

$$\cos(\theta_H - \alpha) = \cos\left(\theta_T + \frac{\pi}{2} + \tan^{-1}\lambda - \alpha\right) = 0,$$

which determines the location of both the grazing bifurcation for hard reset and the saddle-node bifurcation for soft reset. Near these boundaries, a negative slope can result either from $A_S < 0$ or from $A_S \approx 0$ and $A_{C1} < 0$ or $A_{C2} < 0$.

We show the slope $\widehat{H}'_{odd}(0)$ for the full parameter space in Figure 5.2, with the negative slope region highlighted by zooming in near the spiking boundary (Figure 5.2b). Additionally, because the slope $\widehat{H}'_{odd}$ scales with the diverging PRC amplitude A, both negative and positive slopes near these boundaries can grow extremely large. We note, however, that this result should be interpreted with caution, as the assumption of weak coupling also breaks down approaching these boundaries.

The other significant trend in the slope, determining the robustness of synchrony, is the difference between the positive and negative reset regimes. The slope is roughly unit magnitude in the positive reset regime, sharply contrasting with the negative reset regime where the slope is uniformly small (Figure 5.2). By explicitly plotting the slope against the reset point v_R in Figure 5.3, we can see clearly the presence of two regimes with a distinct transition in between. As shown in Figure 2.1a, these two regimes have characteristic voltage waveforms. A large positive v_R is characterized by a plateau potential in the voltage trajectory, while large negative v_R is characterized by after-hyperpolarization (AHP). We conclude that for the resonate-and-fire model in the plateau potential regime, the subthreshold dynamics significantly contribute to synchrony through electrical coupling. In the AHP regime, on the other hand, synchrony is stable for identical intrinsic frequencies but minimally robust to heterogeneity. Because there is little to no subthreshold contribution to synchrony in this regime, the model can only synchronize in the presence of moderate frequency heterogeneity through the effect of the transmitted spike (see section 5.3).

We can further investigate this trend through our slope approximation (5.3), focusing on the S component as the dominant slope contribution. As v_R is increased, the coefficient A_S varies little, while $\hat{S}'_{odd} \approx T - \sin T$ increases sharply with an increase in the period T. That is, increasing the reset voltage v_R increases the angular extent of the limit cycle as it covers more of the (v, w) plane. Note that with $W = 1$ fixed, T represents two distinct factors: the extent of the cycle in radians and its duration. However, varying the duration alone by simply rescaling time has no effect on the strength or robustness of synchrony. The effects represented by H_{odd} are entirely due to the extent of the limit cycle covering a larger fraction of a cycle of continuous oscillation.

5.3. Spike interaction function.

The spiking component of the interaction function also has a significant odd component and thus contributes to the synchronization of the coupled pair. We show here that this contribution always promotes synchrony, reinforcing previous results for excitatory pulse coupling of resonant neurons [47].

In the narrow spike limit implied by the δ-function spike, the interaction function convolution equation (3.12) has a simple form for the spiking component, namely a time-reversed copy of the PRC.[8]

$$
\begin{aligned}
H_{spike}(\phi) &= \frac{M}{T} \int_0^T Z_v(t)\delta(t + \phi)dt \\
&= \frac{M}{T} Z_v(T - \phi) \\
&= \frac{MA}{Tr_0} e^{\lambda(T - \phi)} \cos(\phi - \alpha).
\end{aligned}
$$

Since the spike interaction function is discontinuous at zero, its contribution to the stability and robustness of the synchronous state depends primarily on the size and direction of the discontinuity.[9] The jump discontinuity can stabilize the fully synchronous state even with nonzero heterogeneity if $|\omega_{1-2}| < H_{odd}(0^+) = H_{spike}$ [28, 70, 98]. (For more in-depth analysis of the limit approaching discontinuity in the interaction function, see [98, 52].) We evaluate this discontinuity directly from the PRC:

$$
\begin{aligned}
\Delta H_{spike} &= H_{spike}(0^+) - H_{spike}(0^-) \\
&= \frac{M}{T}\left(Z_v(T^-) - Z_v(0^+)\right), \\
\Delta H_{spike} &= \frac{MA}{Tr_0}\left(e^{\lambda T}\cos\alpha - \cos(T - \alpha)\right).
\end{aligned}
$$

The condition $H_{spike} > 0$ is always satisfied for stable spiking limit cycles in both hard and soft reset conditions. Specifically, $e^{\lambda T}\cos a - \cos(T - a) > 0$ holds for both hard and soft

---

[8]For spike shapes following any smooth function with compact support, the spike interaction function H_{spike} will converge pointwise (for $\phi = 0$) to the H_{spike} resulting from a δ-function in the small-width limit if the charge transfer is held constant. While $H_{spike}(0)$ is left undefined, this single point does not affect synchronization.

[9]If the amplitude of H_{spike} is extremely large relative to H_{sub}, it can create multiple local maxima of the interaction function, allowing multiple stable states. In this case, our analysis still applies to the synchronous phase-locked state, while other locked states would require additional analysis.

reset ($a = 0$ and the phase shift (4.10), respectively), while the scaling factor A changes sign with $\cos(\theta_H - a)$ at the stability boundary (4.5). We evaluate the value of H_{spike} over the full parameter space in section A.7. The spike interaction function thus always promotes the stability of the synchronous state, potentially synchronizing heterogeneous oscillators even when the subthreshold contribution is not synchronizing. As we showed above, the subthreshold contribution to the slope $H'_{odd}(0)$ is near zero or negative for a significant portion of the parameter space, including most of the AHP regime, thus requiring this spike contribution in order to synchronize.

We note that without the assumption that coupling effects are blocked during the spike (discussed in section 2.5), the spike interaction function would have an additional constant term from $Z_v(0)$, the sensitivity to the coupling current that leaves the cell during its spike. The resulting constant offset to the interaction function would only affect synchronization in asymmetrically coupled networks, shifting the effective frequency of each cell by an amount proportional to the total strength of its connections.

6.   Synchronization of a three-cell network: Effect of the even component.

Due to the symmetry of the coupled pair, the odd component of the interaction function alone determines the evolution of the phase difference, and the even-symmetric component has no effect on synchronization. However, the even component has the potential to strongly affect synchronization in both larger resonate-and-fire model networks and actual biological networks. Although many studies of synchronization in model neurons ignore this possibility by focusing on symmetrically coupled pairs, a few studies have described effects of the even component on synchronization [44]. Additionally, mathematical studies of networks of phase oscillators provide significant insight into the potentially complex effects of the even component, typically in the context of large networks [2, 34, 37, 61, 93, 94, 86]. Here, we show that similar effects can be seen in minimal networks, specifically asymmetrically coupled pairs and three-cell networks, the study of which can help us understand the more complex properties of larger networks.

We first provide intuition for the effects of the even component by revisiting the dynamics of a coupled pair, relaxing the previous assumption of symmetric electrical coupling. We express the dynamics of the pair in terms of the phase difference ϕ_{1-2}, coupling asymmetry k, and mean values of the phase $\bar{\theta}$, frequency $\bar{\omega}$, and coupling $\bar{k}$:

$$\frac{d\phi_{1-2}}{dt} = \Delta\omega_{1-2} - 2\bar{k}H_{odd}(\phi_{1-2}) + \Delta k H_{even}(\phi_{1-2}),$$
$$\frac{d\bar{\theta}}{dt} = \bar{\omega} + 2\bar{k}H_{even}(\phi_{1-2}).$$

(6.1)

In the symmetrically coupled pair ($k = k_{12} - k_{21} = 0$), the even component has no effect on the phase difference, but it does shift the frequency $\frac{d\bar{\theta}}{dt}$ of the phase-locked state. In the case of asymmetric coupling strength $k_{12} \neq k_{21}$, the term $kH_{even}(\phi)$ can be interpreted as a differential shift in the instantaneous frequencies of the two oscillators. This effective

frequency shift can either promote or oppose synchrony depending on whether the sign of the product adds to or cancels the intrinsic frequency heterogeneity ω_{1-2}.

In a three-cell network, an even component term in the phase difference dynamics can also arise from coupling to a third oscillator with a different intrinsic frequency, even if the coupling is fully symmetric. The phase difference equation for a symmetric three-cell network with uniform coupling $k_{ij} = K$ is

$$\frac{d\phi_{i-j}}{dt} = \Delta\omega_{i-j} + K\left(\underbrace{H(-\phi_{i-j}) - H(\phi_{i-j})}_{-2\hat{H}_{odd}} + H(-\phi_{i-k}) - H(\phi_{i-j} - \phi_{i-k})\right).$$

While the first two H terms partially cancel to isolate the odd component, the latter two terms depend essentially on the even component. We will first demonstrate the effects of these additional even component terms on phase-locking, along with the effective frequency shifts from coupling asymmetry, in the context of three-cell networks. We will then return to the electrically coupled resonate-and-fire model, investigating the size of the even component of the subthreshold interaction function, its potential effects on neuronal networks, and its origin in the model dynamics.

6.1. Phase-locking of three cells.

A network of three cells is a minimal case that allows network asymmetry (of coupling or frequency) to trigger an effect of the even component even when the pairwise coupling is symmetric. In this context, the amplitude of the odd component (relative to the heterogeneity) is still the primary factor determining the existence of synchronous phase-locking, but the addition of an even component can modify the outcome dramatically, especially when the amplitude of the even component is large relative to that of the odd component.

The phase model for the three-cell network takes the general form of (3.10). We assume pairwise symmetry of the coupling, $k_{ij} = k_{ji}$, and expand the phase difference equations for the network,

$$\begin{aligned}
\dot{\phi}_{1-3} &= \Delta\omega_{1-3} + k_{21}H(-\phi_{1-2}) + k_{31}H(-\phi_{1-3}) - k_{31}H(\phi_{1-3}) \\
&\quad - k_{23}H(\phi_{1-3} - \phi_{1-2}), \\
\dot{\phi}_{1-2} &= \Delta\omega_{1-2} + k_{31}H(-\phi_{1-3}) + k_{21}H(-\phi_{1-2}) - k_{21}H(\phi_{1-2}) \\
&\quad - k_{23}H(\phi_{1-2} - \phi_{1-3}).
\end{aligned} \tag{6.2}$$

To simplify calculations in this analysis, we restrict the interaction function to its first Fourier components,[10]

$$\widehat{H}(\hat{\phi}) = A_{odd}\sin\hat{\phi} + A_{even}(1 - \cos\hat{\phi}), \tag{6.3}$$

---

[10] For the electrically coupled resonate-and-fire subthreshold interaction function, higher modes of the Fourier expansion contribute no more than 6% of the variance of the interaction function for dynamics within the parameter spaces shown (in Figure 5.2 and Figure 6.4, with $\lambda = 0.1$). This approximation may break down for stronger decay.

where $\hat{\phi}$ and $\widehat{H}$ indicate phase in radians (note that we drop the hat notation below). We also impose the constraint that the cosine be accompanied by a constant offset, $H_{even} \propto 1 - \cos \phi$, from the diffusive coupling condition $H(0) = 0$. We parametrize the amplitude of the even component by fixing the odd component and varying the amplitude ratio,

$$\beta = \tan^{-1}\frac{A_{even}}{A_{odd}}.$$

Examples of the two-dimensional phase plane from (6.2) are shown in Figure 6.1a for the phase reduction of the electrically coupled resonate-and-fire model on a *symmetric* three-cell network (approximated in the form (6.3)). The intersections of the nullclines are fixed points of the system, corresponding to phase-locked states. For $\beta = 0$, the odd coupling strength A_{odd} is set at the critical value for phase-locking of the network. Oscillators 1 and 2 are closely locked, while 1 and 3 are locked at $\phi_{1-3} \approx \frac{\pi}{2}$. For small changes in the even component, $\beta > 0$ shifts the nullclines together to promote phase-locking, while $\beta < 0$ shifts them apart. Corresponding simulations of the full resonate-and-fire model network are shown in Figure 6.1b. For $\beta < 0$, oscillators 1 and 2 remain entrained, but oscillator 3 slips past in relative phase.

In a general three-cell network with arbitrary connection weights, this shift of the nullclines combines with the synchronizing effect of the odd component and with the effective heterogeneity from coupling asymmetry to determine the presence or absence of phase-locking. In the limit of small β, we can show analytically that the shift of the nullclines described above is the generic first-order effect on symmetric networks and separates additively from the frequency and coupling heterogeneity terms when both are present. To do this, we first simplify the form of the nullclines by rewriting the coupling as a phase lag accompanied by an offset,

$$H(\phi) = A_{odd}(\sin\phi + \tan\beta(1 - \cos\phi)) \approx A_{odd}(\sin(\phi - \beta) + \beta). \tag{6.4}$$

Taking one of the nullcline equations from (6.2), we then combine all the coupling terms into a single sine function, capturing parametric dependence of the nullcline in the offset, amplitude, and phase of this effective interaction.

$$0 = \frac{\Delta\omega_{1-3}}{A_{odd}} + \omega_{eff} + f_C + f_A\sin(\phi_{1-3} + f_\alpha), \tag{6.5}$$

with the parameters approximated to order β as

$$\omega_{eff} \approx (k_{21} - k_{23})\beta,$$
$$f_C \approx -k_{21}\sin(\phi_{1-2} + \beta),$$
$$f_A \approx -\sqrt{k_{23}^2 + 4k_{31}^2 + 4k_{23}k_{31}\cos(\phi_{1-2} + \beta)},$$
$$f_\alpha \approx \arctan\left(\frac{-k_{23}\sin(\phi_{1-2} + \beta)}{2k_{31} + k_{23}\cos(\phi_{1-2} + \beta)}\right).$$

The amplitude of the odd component appears only in the term $\frac{\Delta\omega_{1-3}}{A_{odd}}$, decreasing the effect of the intrinsic frequency heterogeneity (i.e., larger coupling is equivalent to smaller heterogeneity). When the coupling asymmetry term is small, decreasing the frequency heterogeneity term can be shown to increase the extent of the nullclines, promoting a fixed point as with the coupled pair. The frequency shift term ω_{eff} gives the effective heterogeneity from coupling asymmetry. Similar to the asymmetrically coupled pair (6.1), this supports or opposes phase-locking depending on its sign relative to the intrinsic heterogeneity ω_{1-3}.

The remaining terms represent the additional effects of the even component through their joint dependence on β and ϕ_{1-2}, which for small β reduces to a dependence on the sum (ϕ_{1-2} + β). In a network with symmetric coupling (ω_{eff}= 0), this dependence on (ϕ_{1-2} + β) causes the ϕ_{1-3} nullcline to shift along the ϕ_{1-2} axis with a change in β (and likewise for the ϕ_{1-2} nullcline with respect to ϕ_{1-3}). In the absence of frequency heterogeneity, the nullclines are straight lines $\phi_{1-3} = 0$ and $\phi_{1-2} = 0$ (see (6.2)) and thus are unaffected by these shifts. For larger frequency heterogeneity, the nullclines form closed curves, and a phase-locked fixed point can be lost in a saddle-node bifurcation if the shifts move the nullclines apart. This can occur near the bifurcation for a small change in β of the proper sign (relative to the frequency heterogeneity) as shown in Figure 6.1, or for larger changes in β regardless of sign. As β grows larger, the shift of the nullclines increases proportionally (accompanied by distortion from higher order terms not included in (6.5)). An example where this larger shift eliminates the synchronous fixed point regardless of the sign of β is shown in Figure 6.2.

We next investigate which effects of the even component occur generically for random networks versus contingent on the specific coupling and frequencies. This may provide insight into larger network dynamics, to the extent that global synchrony of a large network can act to average the synchrony of random subnetworks. In Figure 6.3 we plot the Kuramoto order parameter $R^2 = \frac{1}{N_t}\sum_t |\frac{1}{N_j}\sum_j e^{i\phi_j(t)}|^2$, a measure of the strength of synchrony, averaged over time and over instantiations of random frequencies and coupling heterogeneity. Effects that depend on the sign of β (relative to the frequency or coupling heterogeneity) are averaged out; we see no effect for small β of either the nullcline shifts or the coupling asymmetry effects. For sufficiently large β, we see a significant decrease in synchrony with both types of heterogeneity, as the even component effects begin to dominate over the intrinsic frequency heterogeneity (as in Figure 6.2). This result resembles analytical results for chains of oscillators with spatially constrained coupling, where an increase in the critical coupling occurs for $\beta \geq \frac{\pi}{4}$ [84, 111]. It should be noted that in large networks the effect of the even component on synchronization can depend dramatically on the probability distribution from which the frequencies are drawn [83], whereas this dependence for random three-cell networks is minimal.

6.2. Even component of subthreshold interaction function.

In the previous section we showed that the even component of the interaction function can have significant effects on phase-locking. We now proceed to assess the magnitude of the

even component for the electrically coupled resonate-and-fire oscillator. In Figure 6.4, we plot the amplitude ratio β of the even component for the subthreshold interaction function. We note a dramatic difference between the positive and negative reset regimes (as seen with the odd component slope in Figure 5.2). β is consistently large and negative in the negative reset regime (except for a small positive region for soft reset where the odd component is negative) and varies significantly across the positive reset regime. Although both the odd and even amplitudes decrease with v_R (towards $v_R = -1$), the odd component remains smaller, explaining the large amplitude ratio in the negative reset regime. However, since the overall amplitude of the subthreshold interaction function is small, any effects of the even component here are likely to be dominated by the spike interaction, as discussed in section 5.3. In the positive reset regime, both the overall and relative amplitudes can be significant. β increases from negative to positive with increases in v_{eq} and is largest in magnitude at the spiking regime boundaries. This trend is driven by the component function $C1$ from (4.13), for which the coefficient $A_{C1} \approx \frac{A}{2} v_{eq}$ (for hard reset). The component function $C2$ also contributes to the even component, but to a lesser degree.

Where the even component is small in magnitude (Figure 6.4, green region) the effects depend on the sign of β and cancel when averaged over random networks. Small even components are thus unlikely to significantly affect large biological networks. For the tuning of local connection properties to overcome this averaging and support or oppose synchrony, the even component of a connection would need to be tuned based on the frequencies and coupling strengths of both coupled cells, a possibility that seems biologically unrealistic. However, the even component is sufficiently large in a significant portion of the parameter space to potentially oppose synchrony in random networks (as in Figure 6.3). In the neural context, for systems in which synchrony supports biological function, cells may need to adapt their dynamical properties to keep the even component small. This can occur most directly through shifting the equilibrium v_{eq}, either by slower changes in conductances or synaptic weights, or by faster shifts in the tonic input to the cell. This mechanism could potentially enable rapid adaptive shifts (up or down) in the level of synchrony. Finally, it is possible that a large even component could instead promote specific functional states, such as a chimera state [66], rather than simply opposing synchrony.

6.3. Origin of the even component.

Due to a predominant focus on odd component effects and symmetric coupling contexts, the literature on neural synchrony has little discussion of the factors determining variation in the even component. Thus, with the goal of illuminating this broader question, we present a brief analysis for the electrically coupled resonate-and-fire model, explaining the origin of phase shifts of the interaction function relative to the purely odd case. We consider an approximation in which the limit cycle, PRC, and resulting interaction function are all sinusoidal, differing only in phase shifts. (This is strictly true only in the small decay and large period limit.) The phase of the interaction function follows from the relative phase of v and Z_v, determined by the boundary condition (3.14) for the adjoint equation. For the hard reset, if the limit cycle crosses the threshold at $\theta_T \approx 3\pi/2$ ($v_{eq} \approx 0$), v and Z_v are out of phase by $\approx \frac{\pi}{2}$, resulting in an odd interaction function $H \approx \sin$. Any phase shift in the PRC away

from this produces a corresponding shift of the interaction function, introducing a nonzero even component. This can occur if v_{eq} shifts away from 0, or from the soft reset boundary condition phase shift a.

A more geometrical perspective on the relative phase of the limit cycle and PRC is through the concept of dynamical *shear*, variation of angular velocity with radial displacement from a limit cycle. In a model without shear, perturbations perpendicular to the cycle do not cause phase shifts, so the limit cycle is parallel to the (vector) PRC. This is close to the condition that components of the limit cycle and PRC be $\frac{\pi}{2}$ out of phase, and tends to lead to an odd interaction function for diffusive coupling. For instance, in the Stuart–Landau oscillator, a minimal model for shear about a limit cycle, the shear term in the dynamics directly scales a cosine term in the interaction function [4]. In the resonate-and-fire model, although there is no shear in the linear subthreshold dynamics, the effect of the threshold shifts the orientation of the vector PRC relative to the limit cycle exactly like shear in the Stuart–Landau oscillator. This effective "reset-induced shear" is caused by perturbed trajectories on one side of the limit cycle crossing threshold earlier than those on the other side. In the soft reset case, this effect also depends on the geometry of the reset manifold. We can assess the validity of this explanation by evaluating a condition for no shear in the resonate-and-fire model. Radial perturbations have no effect on phase when the PRC is perpendicular to the radial direction, or parallel to the PRC,

$$Z(t) \propto \frac{dx}{dt}(t) \,. \tag{6.6}$$

In Figure 6.4, we show condition (6.6) for zero reset-induced shear as a dotted line. We see that this intuition breaks down in the negative reset regime, where the odd component is extremely small. Otherwise, the condition closely approximates $\beta = 0$, with small variations that result from effects of the discontinuities in v and Z_v not accounted for in this analysis.

7. Discussion.

We applied the theory of weakly coupled oscillators to study the synchronization of resonate-and-fire neurons coupled by electrical synapses. The use of a minimal hybrid model to capture a range of post-spike subthreshold dynamics allowed many conclusions to be established analytically. We calculated the phase reduction of the resonate-and-fire model neuron using the adjoint method for the PRC of hybrid models, following Shirasaka, Kurebayashi, and Nakao [98] and Park et al. [87]. We also presented a simplified derivation of their technique. We found that the post-spike reset voltage determines a potentially strong contribution of the resonant subthreshold fluctuations to synchronization, in addition to the synchronizing effect of the spike. We also showed that, despite having no effect on coupled pairs, effects arising from the reset (i.e., reset-induced shear) have the potential to impair synchronization in certain network configurations.

7.1 Synchronization of electrically coupled resonate-and-fire oscillators.

Our analysis focused on the resonate-and-fire oscillator as an idealized model to study synchronization of electrically coupled resonant neurons with a wide range of post-spike

dynamics. The phase reduction technique allowed us to separate the interaction function into components from spiking and subthreshold voltage fluctuations, dissecting their distinct contributions to synchronization. We focus primarily on the subthreshold contribution, which varies strongly with the parameters of the reset. In coupled pairs and other networks with extensive symmetry, synchronization is solely determined by the odd component of the interaction function. For the electrically coupled resonate-and-fire model, the subthreshold contribution to this odd component generally has a positive slope, promoting stable synchrony. This subthreshold contribution is small when the reset voltage v_R is strongly negative, corresponding to AHP. A stronger synchronizing contribution occurs when v_R is well above threshold, corresponding to a plateau potential. The only significant departures from this rule are strong subthreshold effects near the boundaries of the spiking regime, including the small region with desynchronizing effects. However, the assumption of weak coupling breaks down near these bifurcations, so this conclusion should be verified by different methods of analysis.

In our analysis of the resonate-and-fire model spike contribution, we showed that the effect of a fast voltage spike transmitted through electrical coupling is always synchronizing, reinforcing previous work on pulse coupling of resonant neurons [47, 64, 33, 102]. Where the spike and subthreshold synchronizing effects oppose one another, our model predicts that the net effect will depend linearly on the relative magnitude of the subthreshold fluctuations and the spike. Although our model does not explore the factors determining spike size, a more quantitative analysis of the resonate-and-fire spike effects could integrate spike size measurements obtained from experiments or from detailed biophysical models.

Finally, we showed that in networks with sufficient asymmetry, significant reset-induced effects on synchronization can appear. The even component of the interaction function is often ignored in the neural context, both because analyses focus on symmetrically coupled pairs (e.g., [70]) and because, as observed by Sakaguchi, Shinomoto, and Kuramoto [94], it has complex "ambivalent effects on mutual entrainment." (However, see [61, 86].) We analyze three-cell networks of generic phase oscillators to show how the even component has the potential to oppose synchrony, especially when large enough to dominate over intrinsic frequency heterogeneity. In the electrically coupled resonate-and-fire model, the even component varies strongly with the equilibrium voltage or applied current, potentially interfering with the subthreshold synchronizing effect in parts of the positive reset regime. In general, any phase shift of the interaction function will introduce an even component; our derivation of the adjoint method for hybrid model PRCs clarifies a mechanism for such phase shifts linked to the post-spike reset. The boundary condition for the hybrid PRC determines the phase shift, dependent on the reset map (hard or soft reset) and on the geometry of the trajectory, threshold, and reset manifold. We characterize this effect as "reset-induced shear": a phase shift results when trajectories on one side of the limit cycle cross threshold and are reset ahead of the limit cycle trajectory.

7.2 Comparison of resonator and integrator neurons.

Taken as a whole, our results show that subthreshold resonance of model neurons can have a significant synchronizing effect in electrically coupled networks, by enabling significant

post-spike voltage fluctuations not typically found in integrator neuron dynamics. Previous work on single-variable integrate-and-fire models has found that the subthreshold effect of electrical coupling tends to oppose synchrony [69, 89]. Because the reset voltage must be below threshold, the effect of the reset is desynchronizing [70] and tends to dominate the small synchronizing effects of other subthreshold fluctuations. Thus, in simple integrator models synchronization must rely on transmission of the spike only, as with the resonate-and-fire model in the more integrator-like AHP regime. The observation that electrically coupled resonator neurons may additionally rely on continuous subthreshold coupling to synchronize may help explain the loose correlation across brain regions between resonant properties of neurons and the prevalence of electrical synapses found in experiments [51, 88].

We found that the subthreshold contribution to synchrony is strongest in the plateau potential regime. Since the PRC is not dramatically different between the plateau and AHP regimes, our analysis suggests that the subthreshold synchronizing effect of resonance is mediated primarily by the temporal extent of the voltage fluctuations. In the plateau regime the subthreshold voltage waveform extends close to a full sinusoidal cycle, providing greater opportunity for exchange of current. This synchronizing effect likely extends beyond our resonate-and-fire analysis to the electrical coupling of other resonator neurons. Experimental results show plateau potentials in resonant neurons with widespread electrical coupling in the inferior olive [72, 75], suggesting a potential synchronizing effect of the plateau. Synchronization of subthreshold oscillations in the absence of spiking [71] may also rely on a similar mechanism. Our predictions concerning resonance and subthreshold effects are directly testable experimentally, using pharmacological manipulation of resonant properties or dynamic clamp techniques to perturb and test single neurons and circuits.

We note, however, that integrator versus resonator is not a strict classification and does not always correspond directly with synchronization properties, despite the general trends observed. Although type I excitability (associated with a saddle-node on invariant circle (SNIC) bifurcation), type I PRCs (Z_V strictly positive), and the integration of input are often taken as loosely equivalent properties, Ermentrout, Glass, and Oldeman [39] clarified that systems near a SNIC bifurcation can have type II PRCs, with strong negative lobes. Additionally, Dodla and Wilson [28], analyzing synchrony based only on the shapes of the PRC and voltage fluctuations, emphasize that the type of PRC alone is insufficient to determine the synchronization of electrically coupled oscillators. Our work reinforces these results, showing that a resonator model can in certain regimes have integrator-like properties, both in the PRC and in the interaction function and synchrony.

7.3 Synchronization of hybrid model neurons.

The shift in perspective to discontinuous hybrid model dynamics enables insights not possible with biophysical models, cleanly separating distinct components of the electrical coupling effects. However, relating these results back to phenomena in more realistic models is critical for understanding the broader implications, especially where the two representations seem to diverge. The discontinuous hybrid model PRC leads to a spike interaction function that is discontinuous at the origin, whereas estimates of the

(infinitesimal) PRCs from real neurons or biophysical models are continuous and approximately zero at the instant of spiking. However, if we smooth a hybrid neuron PRC (or measure the finite-perturbation direct PRC; see Figure A.1a), the negative jump translates to a continuous peak skewed "rightward," to the latter portion of the PRC closely preceding the spike [70]. Realistic PRCs generally show this rightward skew, which gives a synchronizing positive slope to the interaction function, matching the synchronizing effect of the positive resonate-and-fire discontinuity. The skew of the PRC has been shown to vary with adaptation in a range of models and experiments [33], including in hybrid models [89, 64], related to the effects of resonance and reset on the discontinuity in our study. Future work can bridge the gap between hybrid and continuous models by further exploring shared features such as skew in the PRC, as well as considering the effects of wider spikes along with the hybrid model dynamics. To accomplish this will require a careful treatment of the small spike width and instantaneous reset limits. Our assumption of no current exchange during the spike, for example, could be replaced by the more realistic case of low susceptibility following from the model dynamics.

For the subthreshold effects of electrical coupling, the interaction function depends on both the PRC and the limit cycle, allowing for significant variation in both odd and even components to be captured in the simple resonate-and-fire model. Our work reinforces observations that subthreshold electrical coupling effects can vary widely based on intrinsic properties in both hybrid [89, 23] and biophysical models [59, 18, 74], and also emphasizes additional variability in the even component through the reset-induced shear effect. Although the hard versus soft reset distinction does not have a direct analogue in biophysical models, the fact that our resonate-and-fire results are unchanged for these two limiting cases suggests that they hold for other reset maps in this range—even nonlinear reset maps. Our analysis techniques could be directly extended to explore these general reset properties in more depth, potentially linking them back to features of biophysical models in scenarios where they do have direct effects.

Given the many advantages of hybrid models for both analytical understanding and computational efficiency, knowing their limits is critical, but attempts at derivations from more complex biophysical models are challenging and typically give results only for narrow cases [58, 52]. Several studies instead address direct validation of dynamic properties, comparing input response [100, 11], spiking transitions [31], or network spiking dynamics [48] between hybrid and biophysical models. Phase reduction can also provide a locus for such comparison, since detailed models can be phase-reduced computationally, translating them into the same "language" as our study of the resonate-and-fire model. Our separation of spike, subthreshold, and reset effects can also provide insight into biophysically derived phase models, in terms of sets of ion channels that tend to be active in specific segments of the limit cycle, e.g., sodium and potassium for spiking dynamics, slow potassium currents and the hyperpolarization-activated HCN channel for subthreshold dynamics, and calcium-activated currents (KCa or CAN) for post-spike reset dynamics. Our conclusions regarding the synchronization of resonant neurons can thus be verified and extended by comparisons with the computational phase reduction of detailed biophysical models and with the empirical phase response analysis of real neurons.
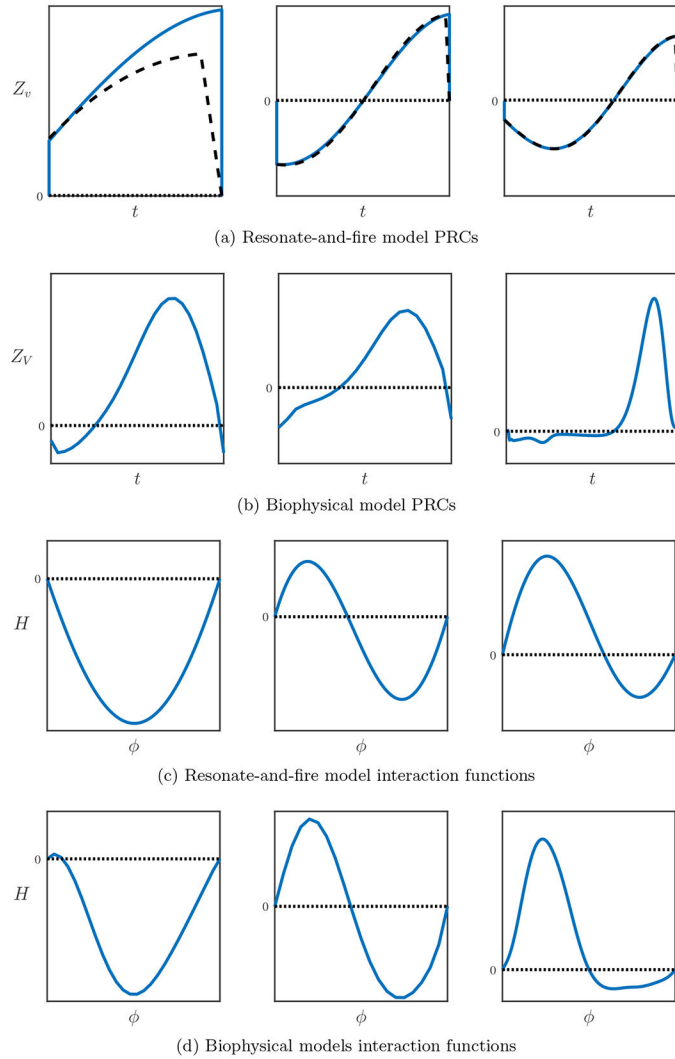
Funding:

Appendix A.: Supplementary analysis and figures.

A.1.   Resonate-and-fire and biophysical model PRC comparison.

Here we provide additional comparison between the resonate-and-fire model with varying reset parameters and a range of biophysical models exhibiting distinct post-spike dynamics. A corresponding comparison of voltage trajectories is shown in Figure 2.1. We calculate the PRCs and electrical coupling interaction functions of all models, illustrating that the resonate-and-fire model captures the essential synchronization properties of the more detailed models. The results are shown in Figure A.1. The cortical cell type models analyzed (left and center) were introduced by [90] to capture general electrophysiological classes observed across many different cortical and thalamic cell types, including electrically coupled networks of inhibitory cortical interneurons [45] and of thalamic reticular cells [43]. The plateau potential example shown (right) is a model from the inferior olive, which also shows widespread electrical coupling [24].

The results in Figure A.1 illustrate that the resonate-and-fire model captures a wide range of post-spike and subthreshold dynamics along with the essential trends in the PRC that accompany these changes. Specifically, although details of relative amplitude are not perfectly matched for all examples, note that the trends in the relative size of the positive and negative lobes of the PRC match closely. The *H*-functions match extremely well for all examples, showing that the features missed by the PRC of the resonate-and-fire model are not essential in determining synchronization in the weak coupling regime.

(a) Resonate-and-fire model PRCs

(b) Biophysical model PRCs

(c) Resonate-and-fire model interaction functions

(d) Biophysical models interaction functions

Figure A.1.
Comparison of phase reduction between resonate-and-fire and biophysical models. Models correspond to cortical cells of fast-spiking (left) and bursting (center) electrophysiological classes, and inferior olive neurons (right). (a), (c) Resonate-and-fire model PRCs $Z_v(t)$ (solid), along with finite-perturbation direct PRC (dashed), and interaction functions $H(\phi)$. (b), (d) Biophysically detailed model (finite-perturbation) PRCs and interaction functions. Resonate-and-fire model parameters (v_{eq}, v_0, w_0) from left to right: $(-1, -1, -1.2)$, $(0, 0, 1)$, $(2, 0, 1)$. $\lambda = 0.1$ for all.

Computational methods for biophysical comparison.

The code for cortical models [90] was obtained from ModelDB [76] (accession number 123623) and simulated in NEURON [16, 50]. Parameters were set as specified for fast-spiking interneurons (IN), with 0.5 nA current input (left); and repetitive bursting (IBR), with 0.15 nA current input (center). The olivary model was implemented and simulated in MATLAB (R2016a) according to the equations and default parameters from [24].

Finite-perturbation phase response curves were calculated following the direct method as

$$Z_V(t) = \frac{\tau(\bar{x}(t)) - \tau(\bar{x}(t) + \Delta V)}{\Delta V},$$ (6.1)

where $\tau(x)$ indicates the time to spiking for a trajectory starting in state x, with the difference evaluated between the regular spiking limit cycle $\bar{x}(t)$ and a trajectory perturbed at time t by an amount ΔV. For the resonate-and-fire model, perturbations were direct shifts in voltage, while for biophysical models, perturbations were implemented as current pulses of 1 ms duration. Spike times were recorded at each upward crossing of a 0 mV threshold. Interaction functions for the biophysical models were computed using the direct PRCs, according to (3.12), assuming linear voltage coupling with a fixed conductance.

A.2.   Connection to Shirasaka, Kurebayashi, and Nakao [98].

Here we will demonstrate that the boundary condition (3.14) for the hybrid model PRC across the reset discontinuity, which we derived in section 3.4, matches the result derived by Shirasaka, Kurebayashi, and Nakao [98] following techniques from nonsmooth dynamical systems theory. The primary difference between the two results is that we present $N-1$ boundary conditions for a reset map R defined on the $(N-1)$-dimensional threshold manifold, while Shirasaka, Kurebayashi, and Nakao defined a reset map Φ in N dimensions (on an open neighborhood of the threshold) and presented N distinct boundary conditions for the adjoint problem. We show here that the $N-1$ conditions corresponding to our result match exactly, and that the remaining condition simply enforces the normalization (3.9) (regardless of the definition of Φ off the threshold manifold).

Their result is formulated in terms of the *saltation matrix C*,

$$Z(T^-) = C^T Z(T^+),$$ (A.1)

$$C = D\Phi - M.$$ (A.2)

This definition is further expanded in terms of the monodromy matrix M,

$$M = \left(D\Phi f(T^-) - f(T^+)\right)\frac{\hat{v}^T}{f_v(T^-)},$$

where f_v is the v-component of the dynamics, $\hat{v}$ is a v-direction unit vector, and T^- and T^+ are the left and right limits of the boundary crossing. The Jacobian $D\Phi$ corresponds to our directional derivatives $D_u R$ along the threshold manifold. The row space of matrix M is the $\hat{v}$ direction only (perpendicular to the threshold), so for any component Z_i along the threshold, M does not contribute to the boundary condition and (A.1) reduces to our result (3.14).

$$Z_i(T^-) = D_i \Phi^T Z(T^+) = D_i R^T Z(T^+).$$ (A.3)

The remaining v-component boundary condition from (A.1) can be shown to simply enforce the normalization condition (3.9). We first evaluate this final component,

$$Z_v(T^-) = \frac{1}{f_v(T^-)}\left(f_v(T^-)D_v\Phi - D\Phi \cdot f(T^-) + f(T^+)\right) \cdot Z(T^+).$$

We then expand $(D\Phi f(T^-)) \cdot Z(T^+)$ as a sum over components $\sum_{i=1}^{N} f_i(T^-)D_i\Phi \cdot Z(T^+)$. If the Nth term is the v-component $f_v(T^-)D_v\Phi \cdot Z(T^+)$, the remaining $N-1$ components along the threshold reduce to $\sum_{i=1}^{N-1} f_i(T^-)Z_i(T^-)$ according to (A.3).

$$f_v(T^-)Z_v(T^-) = \left(f_v(T^-)D_v\Phi - f_v(T^-)D_v\Phi - \Sigma_{i=1}^{N-1}(f_i(T^-)D_i\Phi) + f(T^+)\right) \cdot Z(T^+),$$
$$f_v(T^-)Z_v(T^-) = -\Sigma_{i=1}^{N-1} f_i(T^-)Z_i(T^-) + f(T^+) \cdot Z(T^+),$$
$$f(T^-) \cdot Z(T^-) = f(T^+) \cdot Z(T^+).$$

Thus, we see that the final boundary condition does not depend on the specific definition of the reset map Φ off the threshold manifold and simply enforces that the normalization condition $f \cdot Z = 1$ holds across the reset.

A.3. PRC phase shift for soft reset.

The general form of the resonate-and-fire PRC is

$$Z_v(t) = \frac{A}{r_0}e^{\lambda t}\cos(t - T + \alpha), \ Z_w(t) = \frac{A}{r_0}e^{\lambda t}\sin(t - T + \alpha).$$

The soft reset boundary condition determines the phase shift α as follows:

$$Z_w(T^-) = Z_w(0^+),$$
$$e^{\lambda T}\sin(\alpha) = \sin(\alpha - T),$$
$$\sin T \cos\alpha = \left(\cos T - e^{\lambda T}\right)\sin\alpha,$$
$$\alpha = \arctan\left(\frac{\sin T}{\cos T - e^{\lambda T}}\right).$$

We show the phase shift evaluated over the full resonate-and-fire parameter space in Figure A.2.

A.4. Subthreshold interaction function (H_{sub}).

We present here a brief outline of the integral for the subthreshold component interaction function,

$$H_{sub}(\phi) = \frac{1}{T}\int_0^T Z_v(t)(v(t + \phi) - v(t))dt,$$

with the subthreshold voltage limit cycle v from (2.4) and PRC from (4.7). To simplify this expression, we define $v_d = v - v_{eq} = r_0 e^{-\lambda t} \cos(t + \theta_0)$. Because the limit cycle is discontinuous at the threshold crossing, we must split the integral into two terms around the discontinuity, $t + \phi < T$ and $t + \phi > T$. The latter term is evaluated using $v(t + \phi) = v(t + \phi - T)$, due to the periodicity of the limit cycle. For compactness, we also separate evaluation of the constant term $C = \frac{1}{T}\int_0^T Z_v(t)v_d(t)dt$.

$$
\begin{aligned}
H_{sub}(\phi) &= \frac{1}{T}\int_0^{T-\phi} Z_v(t)v_d(t+\phi)dt + \frac{1}{T}\int_{T-\phi}^{T} Z_v(t)v_d(t+\phi-T)dt - C \\
&= \frac{A}{T}e^{-\lambda\phi}\left[\int_0^{T-\phi}\cos(t-T+\alpha)\cos(t+\phi+\theta_0)dt + e^{\lambda T}\int_{T-\phi}^{T}\cos(t-T+\alpha)\cos(t+\phi-T+\theta_0)dt\right] - C \\
&= \frac{A}{2T}e^{-\lambda\phi}\left[\int_0^{T-\phi}(\cos(\phi+\theta_T-\alpha)+\cos(2t+\phi-T+\theta_0+\alpha))dt \right. \\
&\quad \left. + e^{\lambda T}\int_{T-\phi}^{T}(\cos(\phi+\theta_0-\alpha)+\cos(2t+\phi-2T+\theta_0+\alpha))dt\right] - C, \\
H_{sub}(\phi) &= \frac{A}{2T}e^{-\lambda\phi}\left[(T-\phi)\cos(\phi+\theta_T-\alpha)+\cos(\theta_0+\alpha)\sin(T-\phi)+\phi e^{\lambda T}\cos(\phi+\theta_0-\alpha)\right. \\
&\quad \left. + e^{\lambda T}\cos(\theta_0+\alpha)\sin\phi\right] - C \\
C &= \frac{1}{T}\int_0^T Z_v(t)v_d(t)dt = \frac{A}{2T}(T\cos(\theta_T-\alpha)+\cos(\theta_0+\alpha)\sin T).
\end{aligned}
$$
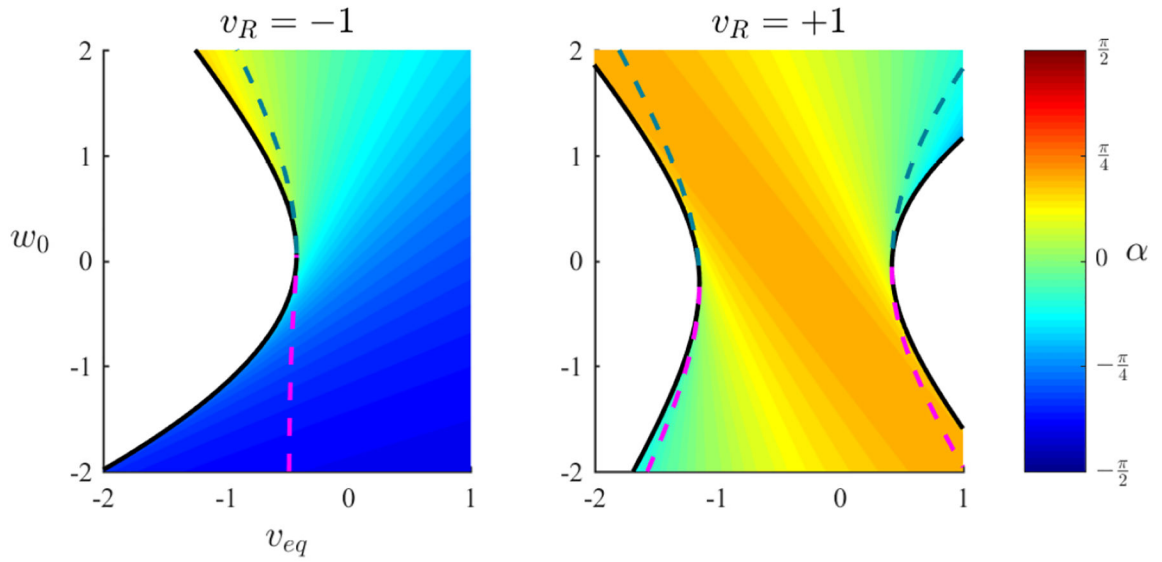
Figure A.2.
Phase shift α of the soft reset PRC Z_v for $\lambda = 0.1$. (Note that $\alpha = 0$ for hard reset.) Magenta and blue-green dashed lines indicate stability boundaries of the limit cycle for positive and negative slope instabilities, respectively.

We then simplify this expression and separate into component functions with distinct parameter dependence.

$$H_{sub}(\phi) = \frac{A}{2T}\Big[\cos(\theta_0 + \alpha)\big(e^{-\lambda\phi}\big[e^{\lambda T}\sin\phi + \sin(T - \phi)\big] - \sin T\big) - T\cos(\theta_T - \alpha) + e^{-\lambda\phi}(T - \phi$$

$$)[\cos\phi\cos(\theta_T - \alpha) - \sin\phi\sin(\theta_T - \alpha)] + e^{-\lambda\phi}e^{\lambda T}\phi[\cos(T - \phi)\cos(\theta_T - \alpha) + \sin(T - \phi)\sin(\theta_T - \alpha)]\Big],$$

$$H_{sub}(\phi) = \frac{A}{2T}\Big[\cos(\theta_0 + \alpha)\big(e^{-\lambda\phi}\big[e^{\lambda T}\sin\phi + \sin(T - \phi)\big] - \sin T\big)$$

$$+ \cos(\theta_T - \alpha)\big(e^{-\lambda\phi}\big[(T - \phi)\cos\phi + e^{\lambda T}\phi\cos(T - \phi)\big] - T\big) + \sin(\theta_T - \alpha)e^{-\lambda\phi}\big[-(T - \phi)\sin\phi + e^{\lambda T}\phi\sin(T - \phi)\big]$$

$$\Big].$$

A.5.   Slope of interaction function components.

Here we evaluate the slope of each component of the resonate-and-fire interaction function and its contribution to the slope of the odd component of the interaction function. We expand the final result to first order in the decay parameter λ. The contributions to the total slope from each component function are scaled by the coefficients

$$A_{C1} = -\frac{A}{2}\cos(\theta_T - \alpha), \; A_{C2} = \frac{A}{2}\cos(\theta_0 + \alpha), \; A_S = -\frac{A}{2}\sin(\theta_T - \alpha).$$

In the calculations below, we use the following result for the slope of the odd component:

$$f_{odd}(\phi) = \frac{1}{2}(f(\phi) - f(T - \phi)),$$

$$f'_{odd}(\phi) = \frac{1}{2}(f'(\phi) + f'(T - \phi)).$$

$$C1(\phi) = 1 - \frac{1}{T}e^{-\lambda\phi}\big[e^{\lambda T}\phi\cos(T - \phi) + (T - \phi)\cos\phi\big],$$

$$C1'(\phi) = \frac{1}{T}e^{-\lambda\phi}\big[-e^{\lambda T}\cos(T - \phi) - e^{\lambda T}\phi\sin(T - \phi) + \lambda e^{\lambda T}\phi\cos(T - \phi) + \cos\phi + (T - \phi)\sin\phi + \lambda(T - \phi$$

$$)\cos\phi\big],$$

$$C1'(0) = \frac{1}{T}\big(-e^{\lambda T}\cos T + 1 + \lambda T\big),$$

$$C1'(T) = \frac{1}{T}\big(-1 + \lambda T + e^{-\lambda T}\cos T\big),$$

$$C1'_{odd}(0) = \lambda - \frac{1}{T}\cos T \sinh(\lambda T) \approx \lambda(1 - \cos T),$$

$$C2(\phi) = \frac{1}{T}e^{-\lambda\phi}\big[e^{\lambda T}\sin\phi + \sin(T - \phi)\big] - \frac{\sin T}{T},$$

$$C2'(\phi) = \frac{1}{T}e^{-\lambda\phi}\big[e^{\lambda T}\cos\phi - \lambda e^{\lambda T}\sin\phi - \cos(T - \phi) - \lambda\sin(T - \phi)\big],$$

$$C2'(0) = \frac{1}{T}\big(e^{\lambda T} - \cos T - \lambda\sin T\big),$$

$$C2'(T) = \frac{1}{T}\big(\cos T - \lambda\sin T - e^{-\lambda T}\big),$$

$$C2'_{odd}(0) = \frac{1}{T}(\sinh(\lambda T) - \lambda\sin T) \approx \lambda\Big(1 - \frac{\sin T}{T}\Big),$$

$$S(\phi) = \frac{1}{T}e^{-\lambda\phi}\Big[-e^{\lambda T}\phi\sin(T-\phi) + (T-\phi)\sin\phi\Big],$$

$$S'(\phi) = \frac{1}{T}e^{-\lambda\phi}\Big[-e^{\lambda T}\sin(T-\phi) + e^{\lambda T}\phi\cos(T-\phi) - \lambda e^{\lambda T}\phi\sin(T-\phi) - \sin\phi + (T-\phi)\cos\phi - \lambda(T-\phi)\sin\phi\Big],$$

$$S'(0) = \frac{1}{T}\Big(-e^{\lambda T}\sin T + T\Big),$$

$$S'(T) = \frac{1}{T}\Big(T - e^{-\lambda T}\sin T\Big),$$

$$S'_{odd}(0) = 1 - \frac{\sin T}{T}\cosh(\lambda T) \approx 1 - \frac{\sin T}{T}.$$

A.6. Amplitude of H_{odd}.

Here we evaluate the *signed amplitude*,

$$SA(H_{odd}) = \text{sign}(H'_{odd}(0))\max|H_{odd}| = H_{odd}(\phi_{\max}),$$
$$\text{where } \phi_{max} = \arg\max_{0 \le \phi \le T/2}|H_{odd}(\phi)|.$$

Just as with the slope $H'_{odd}(0)$, a larger positive signed amplitude implies more robust near-synchronous phase-locking. We plot the signed amplitude of the resonate-and-fire interaction function in Figure A.3; for comparison, see the slope of the interaction function in Figure 5.2. The slope and amplitude are approximately equal,

$SA(H_{odd}) \approx \widehat{H}'_{odd}(0) = \frac{T}{2\pi}H'_{odd}(0)$, as expected from the Fourier approximation

$\widehat{H}_{odd}(\hat{\phi}) \propto \sin(\hat{\phi})$.

A.7. Spike interaction function effect H_{spike}.

Here we assess the discontinuity of the spike interaction function, $H_{spike} = H_{spike}(0^+) - H_{spike}(0^-)$ (section 5.3). We show the spike component discontinuity evaluated over the full resonate-and-fire parameter space in Figure A.4. We see that the discontinuity is positive and relatively constant over the full parameter space, increasing significantly only along the boundaries of the stable spiking regime.
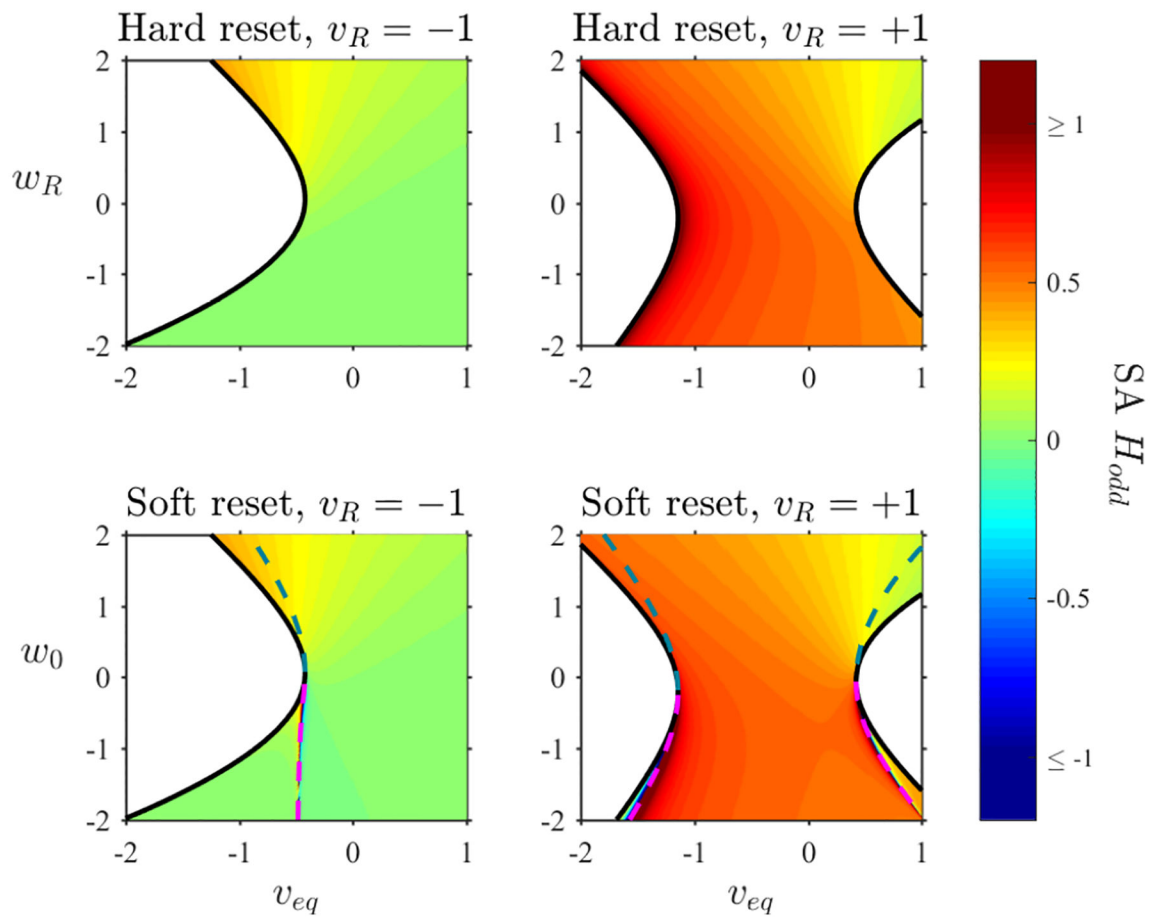
Figure A.3.
Signed amplitude of H_odd, the odd component of the subthreshold interaction function, for λ = 0.1. Magenta and cyan lines indicate stability boundaries of the limit cycle for positive and negative slope instabilities.
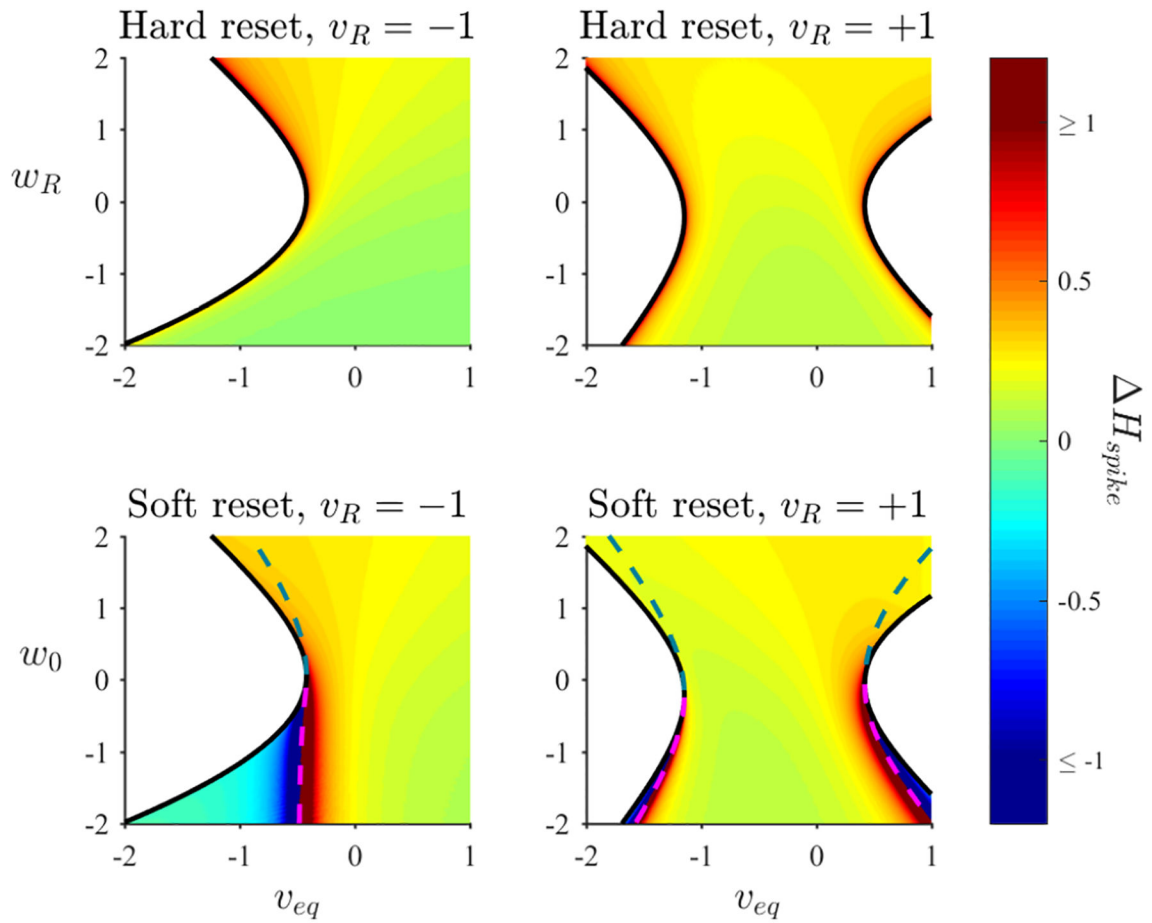
Figure A.4.
Discontinuity of H$_{spike}$, the spike component of the interaction function. Magenta and cyan lines indicate stability boundaries of the limit cycle for positive and negative slope instabilities. Parameters $\lambda = 0.1$, M = 0.2.

REFERENCES

[1]. Abbott LF, Lapicque's introduction of the integrate-and-fire model neuron (1907), Brain Research Bulletin, 50 (1999), pp. 303–304, 10.1016/S0361-9230(99)00161-6. [PubMed: 10643408]

[2]. Acebrón JA, Bonilla LL, Pérez Vicente CJ, Ritort F, and Spigler R, The Kuramoto model: A simple paradigm for synchronization phenomena, Rev. Mod. Phys, 77 (2005), pp. 137–185, 10.1103/RevModPhys.77.137.

[3]. Aizerman MA and Gantmakher FR, On the stability of periodic motions, J. Appl. Math. Mech, 22 (1958), pp. 1065–1078, 10.1016/0021-8928(58)90033-9, 00054.

[4]. Aronson DG, Ermentrout GB, and Kopell N, Amplitude response of coupled oscillators, Phys. D, 41 (1990), pp. 403–449, 10.1016/0167-2789(90)90007-C.

[5]. Ashwin P, Coombes S, and Nicks R, Mathematical frameworks for oscillatory network dynamics in neuroscience, J. Math. Neurosci, 6 (2016), pp. 1–92, 10.1186/s13408-015-0033-6. [PubMed: 26728012]

[6]. Baroni F and Varona P, Spike timing-dependent plasticity is affected by the interplay of intrinsic and network oscillations, J. Physiol.-Paris, 104 (2010), pp. 91–98, 10.1016/j.jphysparis.2009.11.007. [PubMed: 19913095]

[7]. Bennett MVL and Zukin RS, Electrical coupling and neuronal synchronization in the mammalian brain, Neuron, 41 (2004), pp. 495–511, 10.1016/S0896-6273(04)00043-1. [PubMed: 14980200]

[8]. Bernardo M, Budd C, Champneys AR, and Kowalczyk P, Piecewise-Smooth Dynamical Systems: Theory and Applications, Appl. Math. Sci 163, Springer-Verlag, London, 2008.

[9]. Blankenburg S, Wu W, Lindner B, and Schreiber S, Information filtering in resonant neurons, J. Comput. Neurosci, 39 (2015), pp. 349–370, 10.1007/s10827-015-0580-6. [PubMed: 26546022]

[10]. Brette R and Gerstner W, Adaptive exponential integrate-and-fire model as an effective description of neuronal activity, J. Neurophysiol, 94 (2005), pp. 3637–3642, 10.1152/jn.00686.2005. [PubMed: 16014787]

[11]. Brunel N, Hakim V, and Richardson MJE, Firing-rate resonance in a generalized integrate-and-fire neuron with subthreshold resonance, Phys. Rev. E, 67 (2003), 051916, 10.1103/PhysRevE.67.051916.

[12]. Brunel N and Latham PE, Firing rate of the noisy quadratic integrate-and-fire neuron, Neural Comput, 15 (2003), pp. 2281–2306. [PubMed: 14511522]

[13]. Brunel N and van Rossum MCW, Quantitative investigations of electrical nerve excitation treated as polarization, Biol. Cybernet, 97 (2007), pp. 341–349, 10.1007/s00422-007-0189-6.

[14]. Buzsáki G and Draguhn A, Neuronal oscillations in cortical networks, Science, 304 (2004), pp. 1926–1929, 10.1126/science.1099745. [PubMed: 15218136]

[15]. Carmona V, Fernández-García S, Freire E, and Torres F, Melnikov theory for a class of planar hybrid systems, Phys. D, 248 (2013), pp. 44–54, 10.1016/j.physd.2013.01.002.

[16]. Carnevale NT and Hines ML, The NEURON Book, Cambridge University Press, Cambridge, UK, 2006.

[17]. Chen J, Suarez J, Molnar P, and Behal A, Maximum likelihood parameter estimation in a stochastic resonate-and-fire neuronal model, in Proceedings of the 1st IEEE International Conference on Computational Advances in Bio and Medical Sciences (ICCABS), 2011, pp. 57–62, 10.1109/ICCABS.2011.5729941.

[18]. Chow CC and Kopell N, Dynamics of spiking neurons with electrical coupling, Neural Comput, 12 (2000), pp. 1643–1678, 10.1162/089976600300015295. [PubMed: 10935921]

[19]. Connors BW and Long MA, Electrical synapses in the mammalian brain, Annu. Rev. Neurosci, 27 (2004), pp. 393–418, 10.1146/annurev.neuro.26.041002.131128. [PubMed: 15217338]

[20]. Coombes S, Dynamics of synaptically coupled integrate-and-fire-or-burst neurons, Phys. Rev. E, 67 (2003), 041910, 10.1103/PhysRevE.67.041910.

[21]. Coombes S and Bressloff PC, Mode locking and Arnold tongues in integrate-and-fire neural oscillators, Phys. Rev. E, 60 (1999), pp. 2086–2096, 10.1103/PhysRevE.60.2086.

[22]. Coombes S, Thul R, and Wedgwood KCA, Nonsmooth dynamics in spiking neuron models, Phys. D, 241 (2012), pp. 2042–2057, 10.1016/j.physd.2011.05.012.

[23]. Coombes S and Zachariou M, Gap junctions and emergent rhythms, in Coherent Behavior in Neuronal Networks, Josic K, Rubin J, Matias M, and Romo R, eds., Springer Ser. Comput. Neurosci 3, Springer New York, 2009, pp. 77–94.

[24]. De Gruijl JR, Bazzigaluppi P, de Jeu MTG, and De Zeeuw CI, Climbing fiber burst size and olivary sub-threshold oscillations in a network setting, PLoS Comput. Biol, 8 (2012), e1002814, 10.1371/journal.pcbi.1002814. [PubMed: 23271962]

[25]. De Zeeuw CI, Hoogenraad CC, Koekkoek SKE, Ruigrok TJH, Galjart N, and Simpson JI, Microcircuitry and function of the inferior olive, Trends Neurosci, 21 (1998), pp. 391–400, 10.1016/S0166-2236(98)01310-1. [PubMed: 9735947]

[26]. Di Garbo A, Barbi M, and Chillemi S, Dynamical behavior of the linearized version of the Fitzhugh–Nagumo neural model, Internat. J. Bifur. Chaos Appl. Sci. Engrg, 11 (2001), pp. 2549–2558.

[27]. Dodla R and Wilson CJ, Effect of phase response curve skewness on synchronization of electrically coupled neuronal oscillators, Neural Comput, 25 (2013), pp. 2545–2610, 10.1162/NECO_a_00488. [PubMed: 23777519]

[28]. Dodla R and Wilson CJ, Effect of sharp jumps at the edges of phase response curves on synchronization of electrically coupled neuronal oscillators, PLOS ONE, 8 (2013), e58922, 10.1371/journal.pone.0058922. [PubMed: 23555607]

[29]. Dong Y, Mihalas S, Russell A, Etienne-Cummings R, and Niebur E, Estimating parameters of generalized integrate-and-fire neurons from the maximum likelihood of spike trains, Neural Comput, 23 (2011), pp. 2833–2867, 10.1162/NECO_a_00196. [PubMed: 21851282]

[30]. Engel TA, Schimansky-Geier L, Herz A, Schreiber S, and Erchova I, Subthreshold membrane-potential resonances shape spike-train patterns in the entorhinal cortex, J. Neurophysiol, 100 (2008), pp. 1576–1589, 10.1152/jn.01282.2007. [PubMed: 18450582]

[31]. Engelbrecht JR and Mirollo R, Dynamical phase transitions in periodically driven model neurons, Phys. Rev. E, 79 (2009), 021904, 10.1103/PhysRevE.79.021904.

[32]. Erchova I, Kreck G, Heinemann U, and Herz AVM, Dynamics of rat entorhinal cortex layer II and III cells: Characteristics of membrane potential resonance at rest predict oscillation properties near threshold, J. Physiol, 560 (2004), pp. 89–110, 10.1113/jphysiol.2004.069930. [PubMed: 15272028]

[33]. Ermentrout B, Pascal M, and Gutkin B, The effects of spike frequency adaptation and negative feedback on the synchronization of neural oscillators, Neural Comput, 13 (2001), pp. 1285–1310, 10.1162/08997660152002861. [PubMed: 11387047]

[34]. Ermentrout GB and Kopell N, Frequency plateaus in a chain of weakly coupled oscillators, I., SIAM J. Math. Anal, 15 (1984), pp. 215–237, 10.1137/0515019.

[35]. Ermentrout GB and Kopell N, Parabolic bursting in an excitable system coupled with a slow oscillation, SIAM J. Appl. Math, 46 (1986), pp. 233–253, 10.1137/0146017.

[36]. Ermentrout GB, N:m phase-locking of weakly coupled oscillators, J. Math. Biol, 12 (1981), pp. 327–342, 10.1007/BF00276920.

[37]. Ermentrout GB, Synchronization in a pool of mutually coupled oscillators with random frequencies, J. Math. Biol, 22 (1985), pp. 1–9, 10.1007/BF00276542.

[38]. Ermentrout GB, Beverlin B, and Netoff T, Phase response curves to measure ion channel effects on neurons, in Phase Response Curves in Neuroscience, Schultheiss NW, Prinz AA, and Butera RJ, eds., Springer Ser. Comput. Neurosci 6, Springer, New York, 2012, pp. 207–236.

[39]. Ermentrout GB, Glass L, and Oldeman BE, The shape of phase-resetting curves in oscillators with a saddle node on an invariant circle bifurcation, Neural Comput, 24 (2012), pp. 3111–3125. [PubMed: 22970869]

[40]. Ermentrout GB and Kopell N, Multiple pulse interactions and averaging in systems of coupled neural oscillators, J. Math. Biol, 29 (1991), pp. 195–217.

[41]. Fell J and Axmacher N, The role of phase synchronization in memory processes, Nat. Rev. Neurosci, 12 (2011), 105. [PubMed: 21248789]

[42]. Fourcaud-Trocmé N, Hansel D, van Vreeswijk C, and Brunel N, How spike generation mechanisms determine the neuronal response to fluctuating inputs, J. Neurosci, 23 (2003), pp. 11628–11640. [PubMed: 14684865]

[43]. Fuentealba P, Crochet S, Timofeev I, Bazhenov M, Sejnowski TJ, and Steriade M, Experimental evidence and modeling studies support a synchronizing role for electrical coupling in the cat thalamic reticular neurons in vivo, European J. Neurosci, 20 (2004), pp. 111–119, 10.1111/j.1460-9568.2004.03462.x, 00051. [PubMed: 15245484]

[44]. Golomb D and Hansel D, The number of synaptic inputs and the synchrony of large, sparse neuronal networks, Neural Comput, 12 (2000), pp. 1095–1139, 10.1162/089976600300015529. [PubMed: 10905810]

[45]. Gupta A, Wang Y, and Markram H, Organizing principles for a diversity of GABAergic interneurons and synapses in the neocortex, Science, 287 (2000), pp. 273–278, 10.1126/science.287.5451.273. [PubMed: 10634775]

[46]. Gutkin BS, Ermentrout GB, and Reyes AD, Phase-response curves give the responses of neurons to transient inputs, J. Neurophysiol, 94 (2005), pp. 1623–1635, 10.1152/jn.00359.2004. [PubMed: 15829595]

[47]. Hansel D, Mato G, and Meunier C, Synchrony in excitatory neural networks, Neural Comput, 7 (1995), pp. 307–337, 10.1162/neco.1995.7.2.307. [PubMed: 8974733]

[48]. Hansel D, Mato G, Meunier C, and Neltner L, On numerical simulations of integrate-and-fire neural networks, Neural Comput, 10 (1998), pp. 467–483. [PubMed: 9472491]

[49]. Hill AV, Excitation and accommodation in nerve, Proc. Royal Soc. London Ser. B Biol. Sci, 119 (1936), pp. 305–355.

[50]. Hines M, Davison AP, and Muller E, NEURON and Python, Front. Neuroinform, 3 (2009), 00166, 10.3389/neuro.11.001.2009.

[51]. Hutcheon B and Yarom Y, Resonance, oscillation and the intrinsic frequency preferences of neurons, Trends Neurosci, 23 (2000), pp. 216–222, 10.1016/S0166-2236(00)01547-2. [PubMed: 10782127]

[52]. Izhikevich EM, Phase equations for relaxation oscillators, SIAM J. Appl. Math, 60 (2000), pp. 1789–1804, 10.1137/S0036139999351001.

[53]. Izhikevich EM, Resonate-and-fire neurons, Neural Netw, 14 (2001), pp. 883–894. [PubMed: 11665779]

[54]. Izhikevich EM, Simple model of spiking neurons, IEEE Trans. Neural Netw, 14 (2003), pp. 1569–1572. [PubMed: 18244602]

[55]. Izhikevich EM, Which model to use for cortical spiking neurons?, IEEE Trans. Neural Netw, 15 (2004), pp. 1063–1070. [PubMed: 15484883]

[56]. Izhikevich EM, Dynamical Systems in Neuroscience, MIT Press, Cambridge, MA, 2007.

[57]. Jimenez ND, Mihalas S, Brown R, Niebur E, and Rubin J, Locally contractive dynamics in generalized integrate-and-fire neurons, SIAM J. Appl. Dyn. Syst, 12 (2013), pp. 1474–1514, 10.1137/120900435. [PubMed: 24489486]

[58]. Jolivet R, Lewis TJ, and Gerstner W, Generalized integrate-and-fire models of neuronal activity approximate spike trains of a detailed model to a high degree of accuracy, J. Neurophysiol, 92 (2004), pp. 959–976, 10.1152/jn.00190.2004. [PubMed: 15277599]

[59]. Kepler TB, Marder E, and Abbott LF, The effect of electrical coupling on the frequency of model neuronal oscillators, Science, 248 (1990), pp. 83–85. [PubMed: 2321028]

[60]. Khajeh Alijani A, Mode locking in a periodically forced resonate-and-fire neuron model, Phys. Rev. E, 80 (2009), 051922, 10.1103/PhysRevE.80.051922.

[61]. Kopell N and Ermentrout GB, Symmetry and phaselocking in chains of weakly coupled oscillators, Comm. Pure Appl. Math, 39 (1986), pp. 623–660, 10.1002/cpa.3160390504.

[62]. Kopell N and Ermentrout GB, Mechanisms of phase-locking and frequency control in pairs of coupled neural oscillators, in Handbook of Dynamical Systems, Vol. 2, Fiedler B, ed., Elsevier Science, New York, 2002, pp. 3–54.

[63]. Kuramoto Y, Collective synchronization of pulse-coupled oscillators and excitable units, Phys. D, 50 (1991), pp. 15–30, 10.1016/0167-2789(91)90075-K.

[64]. Ladenbauer J, Augustin M, Shiau L, and Obermayer K, Impact of adaptation currents on synchronization of coupled exponential integrate-and-fire neurons, PLoS Comput. Biol, 8 (2012), e1002478, 10.1371/journal.pcbi.1002478. [PubMed: 22511861]

[65]. Ladenbauer J, Lehnert J, Rankoohi H, Dahms T, Schöll E, and Obermayer K, Adaptation controls synchrony and cluster states of coupled threshold-model neurons, Phys. Rev. E, 88 (2013), 042713, 10.1103/PhysRevE.88.042713.

[66]. Laing CR, The dynamics of chimera states in heterogeneous Kuramoto networks, Phys. Nonlinear Phenom, 238 (2009), pp. 1569–1588, 10.1016/j.physd.2009.04.012.

[67]. Lapicque L, Recherches quantitatives sur l'excitation électrique des nerfs traitée comme une polarisation, J. Physiol. Pathol. Gen, 9 (1907), pp. 620–635.

[68]. Leine RI and Nijmeijer H, Dynamics and Bifurcations of Non-Smooth Mechanical Systems, Springer, Berlin, 2004.

[69]. Lewis TJ and Rinzel J, Dynamics of spiking neurons connected by both inhibitory and electrical coupling, J. Comput. Neurosci, 14 (2003), pp. 283–309. [PubMed: 12766429]

[70]. Lewis TJ and Skinner FK, Understanding Activity in Electrically Coupled Networks Using PRCs and the Theory of Weakly Coupled Oscillators, in Phase Response Curves in Neuroscience, Schultheiss NW, Prinz AA, and Butera RJ, eds., Springer Ser. Comput. Neurosci 6, Springer, New York, 2012, pp. 329–359.

[71]. Leznik E, Makarenko V, and Llinás R, Electrotonically mediated oscillatory patterns in neuronal ensembles: An in vitro voltage-dependent dye-imaging study in the inferior olive, J. Neurosci, 22 (2002), pp. 2804–2815. [PubMed: 11923445]

[72]. Llinas R and Yarom Y, Electrophysiology of mammalian inferior olivary neurones in vitro. Different types of voltage-dependent ionic conductances, J. Physiol, 315 (1981), pp. 549–567. [PubMed: 6273544]

[73]. Luccioli S, Olmi S, Politi A, and Torcini A, Collective dynamics in sparse networks, Phys. Rev. Lett, 109 (2012), 138103, 10.1103/PhysRevLett.109.138103. [PubMed: 23030123]

[74]. Mancilla JG, Lewis TJ, Pinto DJ, Rinzel J, and Connors BW, Synchronization of electrically coupled pairs of inhibitory interneurons in neocortex, J. Neurosci, 27 (2007), pp. 2058–2073, 10.1523/JNEUROSCI.2715-06.2007. [PubMed: 17314301]

[75]. Marshall SP and Lang EJ, Inferior olive oscillations gate transmission of motor cortical activity to the cerebellum, J. Neurosci, 24 (2004), pp. 11356–11367, 10.1523/JNEUROSCI.3907-04.2004. [PubMed: 15601942]

[76]. McDougal RA, Morse TM, Carnevale T, Marenco L, Wang R, Migliore M, Miller PL, Shepherd GM, and Hines ML, Twenty years of ModelDB and beyond: Building essential modeling tools for the future of neuroscience, J. Comput. Neurosci, 42 (2017), pp. 1–10, 10.1007/s10827-016-0623-7. [PubMed: 27629590]

[77]. Mihala and Niebur E, A generalized linear integrate-and-fire neural model produces diverse spiking behaviors, Neural Comput, 21 (2009), pp. 704–718, 10.1162/neco.2008.12-07-680. [PubMed: 18928368]

[78]. Mirollo RE and Strogatz SH, Synchronization of pulse-coupled biological oscillators, SIAM J. Appl. Math, 50 (1990), pp. 1645–1662, 10.1137/0150098.

[79]. Miura K and Okada M, Pulse-coupled resonate-and-fire models, Phys. Rev. E, 70 (2004), 021914.

[80]. Miura K and Okada M, Globally coupled resonate-and-fire models, Progr. Theoret. Phys. Suppl, 161 (2006), pp. 255–259.

[81]. Nakada K, Miura K, and Hayashi H, Burst synchronization and chaotic phenomena in two strongly coupled resonate-and-fire neurons, Internat. J. Bifur. Chaos Appl. Sci. Engrg, 18 (2008), pp. 1249–1259, 10.1142/S0218127408020999.

[82]. Naud R, Marcille N, Clopath C, and Gerstner W, Firing patterns in the adaptive exponential integrate-and-fire model, Biol. Cybernet, 99 (2008), 335, 10.1007/s00422-008-0264-7.

[83]. Omel'chenko OE and Wolfrum M, Nonuniversal transitions to synchrony in the Sakaguchi-Kuramoto model, Phys. Rev. Lett, 109 (2012), 164101, 10.1103/PhysRevLett.109.164101. [PubMed: 23215080]

[84]. Omel'chenko OE, Wolfrum M, and Laing CR, Partially coherent twisted states in arrays of coupled phase oscillators, Chaos Interdiscip. J. Nonlinear Sci, 24 (2014), 023102, 10.1063/1.4870259.

[85]. Ostojic S, Brunel N, and Hakim V, Synchronization properties of networks of electrically coupled neurons in the presence of noise and heterogeneities, J. Comput. Neurosci, 26 (2009), pp. 369–392, 10.1007/s10827-008-0117-3. [PubMed: 19034642]

[86]. Panaggio MJ and Abrams DM, Chimera states: Coexistence of coherence and incoherence in networks of coupled oscillators, Nonlinearity, 28 (2015), R67, 10.1088/0951-7715/28/3/R67.

[87]. Park Y, Shaw KM, Chiel HJ, and Thomas PJ, The infinitesimal phase response curves of oscillators in piecewise smooth dynamical systems, European J. Appl. Math, 29 (2018), pp. 905–940, 10.1017/S0956792518000128.

[88]. Pereda AE, Curti S, Hoge G, Cachope R, Flores CE, and Rash JE, Gap junction-mediated electrical transmission: Regulatory mechanisms and plasticity, Biochim. Biophys. Acta, 1828 (2013), pp. 134–146, 10.1016/j.bbamem.2012.05.026. [PubMed: 22659675]

[89]. Pfeuty B, Mato G, Golomb D, and Hansel D, Electrical synapses and synchrony: The role of intrinsic currents, J. Neurosci, 23 (2003), pp. 6280–6294. [PubMed: 12867513]

[90]. Pospischil M, Toledo-Rodriguez M, Monier C, Piwkowska Z, Bal T, Frégnac Y, Markram H, and Destexhe A, Minimal Hodgkin–Huxley type models for different classes of cortical and thalamic neurons, Biol. Cybernet, 99 (2008), pp. 427–441, 10.1007/s00422-008-0263-8.

[91]. Rashevsky N, Outline of a physico-mathematical theory of excitation and inhibition, Protoplasma, 20 (1933), pp. 42–56, 10.1007/BF02674811.

[92]. Richardson MJE, Brunel N, and Hakim V, From subthreshold to firing-rate resonance, J. Neurophysiol, 89 (2003), pp. 2538–2554, 10.1152/jn.00955.2002. [PubMed: 12611957]

[93]. Sakaguchi H and Kuramoto Y, A soluble active rotater model showing phase transitions via mutual entrainment, Progr. Theoret. Phys, 76 (1986), pp. 576–581.

[94]. Sakaguchi H, Shinomoto S, and Kuramoto Y, Mutual entrainment in oscillator lattices with nonvariational type interaction, Progr. Theoret. Phys, 79 (1988), pp. 1069–1079.

[95]. Schwemmer MA and Lewis TJ, Bistability in a leaky integrate-and-fire neuron with a passive dendrite, SIAM J. Appl. Dyn. Syst, 11 (2012), pp. 507–539, 10.1137/110847354.

[96]. Schwemmer MA and Lewis TJ, The theory of weakly coupled oscillators, in Phase Response Curves in Neuroscience, Schultheiss NW, Prinz AA, and Butera RJ, eds., Springer Ser. Comput. Neurosci 6, Springer, New York, 2012, pp. 3–31.

[97]. Sherman A and Rinzel J, Rhythmogenic effects of weak electrotonic coupling in neuronal models, Proc. Natl. Acad. Sci. USA, 89 (1992), pp. 2471–2474. [PubMed: 1549611]

[98]. Shirasaka S, Kurebayashi W, and Nakao H, Phase reduction theory for hybrid nonlinear oscillators, Phys. Rev. E, 95 (2017), 012212. [PubMed: 28208342]

[99]. Singer W, Neuronal synchrony: A versatile code for the definition of relations?, Neuron, 24 (1999), pp. 49–65, 10.1016/S0896-6273(00)80821-1. [PubMed: 10677026]

[100]. Smith GD, Cox CL, Sherman SM, and Rinzel J, Fourier analysis of sinusoidally driven thalamocortical relay neurons and a minimal integrate-and-fire-or-burst model, J. Neurophysiol, 83 (2000), pp. 588–610. [PubMed: 10634897]

[101]. Srinivas M, Rozental R, Kojima T, Dermietzel R, Mehler M, Condorelli DF, Kessler JA, and Spray DC, Functional properties of channels formed by the neuronal gap junction protein connexin36, J. Neurosci, 19 (1999), pp. 9848–9855. [PubMed: 10559394]

[102]. Stiefel KM, Gutkin BS, and Sejnowski TJ, The effects of cholinergic neuromodulation on neuronal phase-response curves of modeled cortical neurons, J. Comput. Neurosci, 26 (2009), pp. 289–301, 10.1007/s10827-008-0111-9. [PubMed: 18784991]

[103]. Teeter C, Iyer R, Menon V, Gouwens N, Feng D, Berg J, Szafer A, Cain N, Zeng H, Hawrylycz M, Koch C, and Mihalas S, Generalized leaky integrate-and-fire models classify multiple neuron types, Nat. Commun, 9 (2018), 709, 10.1038/s41467-017-02717-4. [PubMed: 29459723]

[104]. Touboul J and Brette R, Spiking dynamics of bidimensional integrate-and-fire neurons, SIAM J. Appl. Dyn. Syst, 8 (2009), pp. 1462–1506, 10.1137/080742762.

[105]. Treves A, Mean-field analysis of neuronal spike dynamics, Netw. Comput. Neural Syst, 4 (1993), pp. 259–284.

[106]. Verechtchaguina T, Sokolov IM, and Schimansky-Geier L, Interspike interval densities of resonate and fire neurons, Biosystems, 89 (2007), pp. 63–68, 10.1016/j.biosystems.2006.03.014. [PubMed: 17331639]

[107]. Wedgwood KC, Lin KK, Thul R, and Coombes S, Phase-amplitude descriptions of neural oscillator models, J. Math. Neurosci, 3 (2013), 2, 10.1186/2190-8567-3-2. [PubMed: 23347723]

[108]. Wilson D, Isostable reduction of oscillators with piecewise smooth dynamics and complex Floquet multipliers, Phys. Rev. E, 99 (2019), 022210, 10.1103/PhysRevE.99.022210. [PubMed: 30934292]

[109]. Wilson D and Ermentrout B, Greater accuracy and broadened applicability of phase reduction using isostable coordinates, J. Math. Biol, 76 (2018), pp. 37–66, 10.1007/s00285-017-1141-6. [PubMed: 28547210]

[110]. Wilson D and Moehlis J, Isostable reduction of periodic orbits, Phys. Rev. E, 94 (2016), 052213, 10.1103/PhysRevE.94.052213. [PubMed: 27967132]

[111]. Wolfrum M, Gurevich SV, and Omel'chenko OE, Turbulence in the Ott–Antonsen equation for arrays of coupled phase oscillators, Nonlinearity, 29 (2016), 257, 10.1088/0951-7715/29/2/257.

[112]. Young G, Note on excitation theories, Psychometrika, 2 (1937), pp. 103–106, 10.1007/BF02288064.

(a) Biophysical models

(b) Resonate-and-fire model
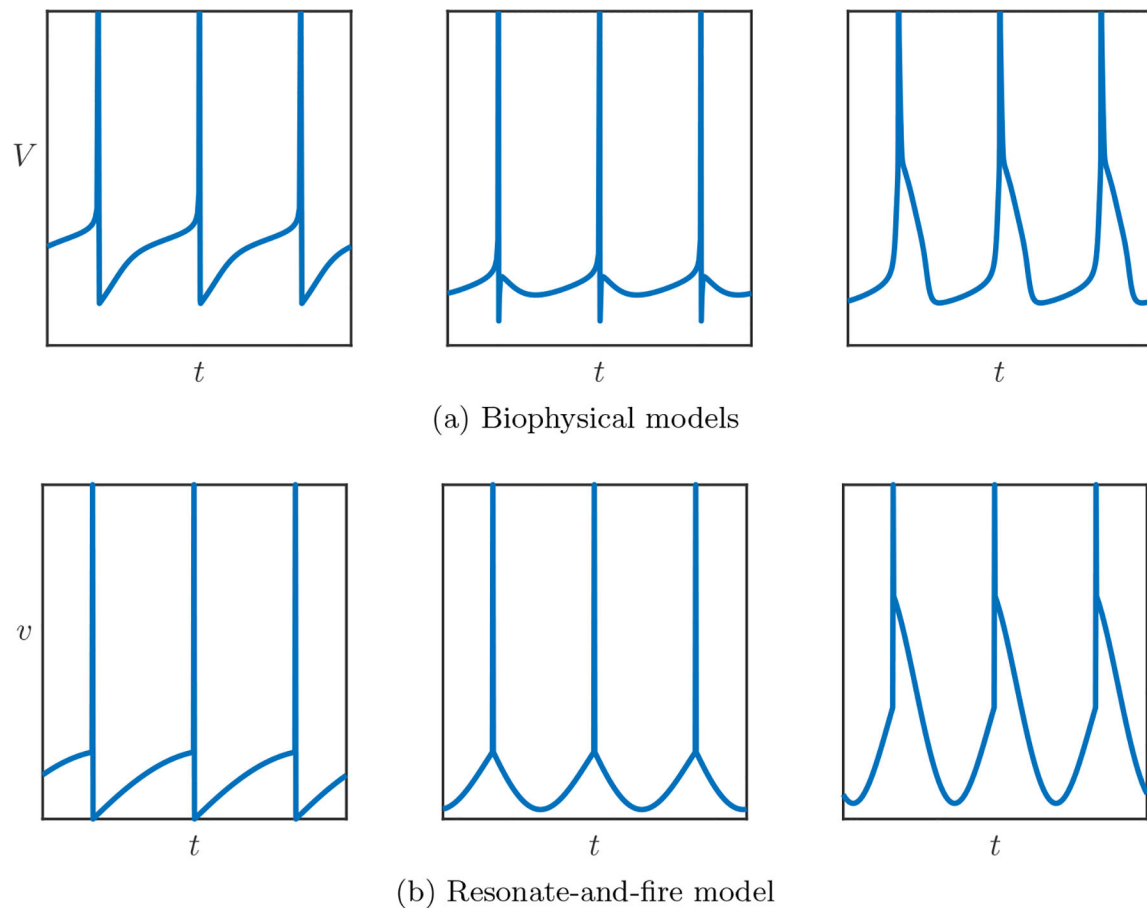
Figure 2.1.
Distinct post-spike dynamics in spiking neurons range from after-hyperpolarization (AHP), either fast (left) or slow (center), to depolarized plateau potentials (right). (a) Voltage trajectories from biophysically detailed models for cortical cells of fast-spiking (left) and bursting (center) electrophysiological classes, and for inferior olive neurons (right). (b) Voltage trajectories of the resonate-and-fire model for different reset parameters. Instantaneous spikes have been added to the subthreshold trajectories to indicate spike times. Resonate-and-fire model parameters (v_{eq}, v_0, w_0) from left to right: $(-1, -1, -1.2)$, $(0, 0, 1)$, $(2, 0, 1)$. $\lambda = 0.1$ for all.
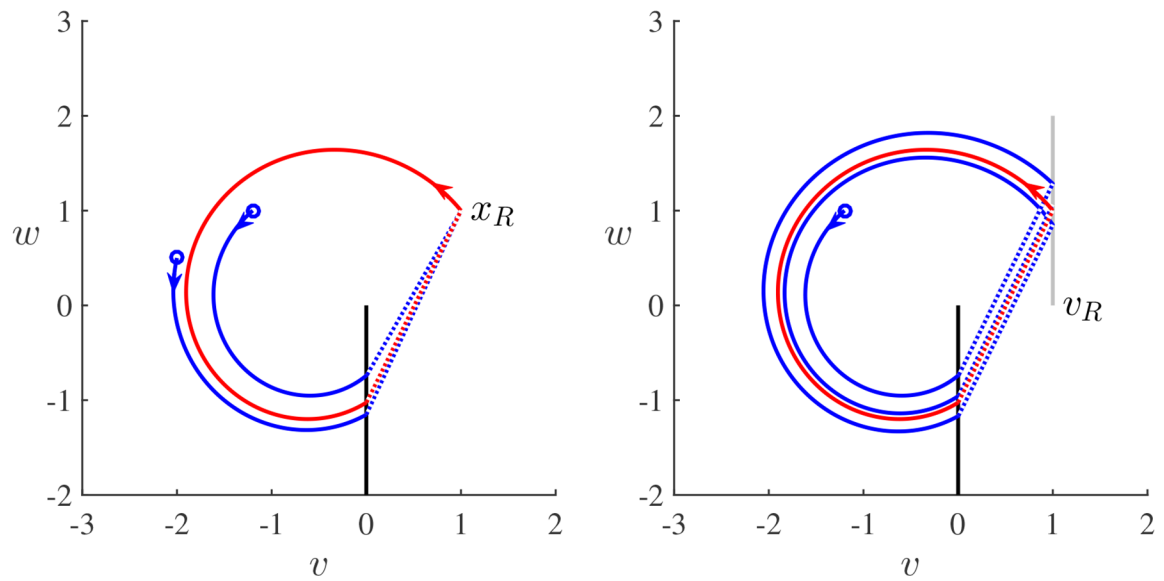
Figure 2.2.
Effects of hard and soft reset maps on resonate-and-fire model spiking trajectories, shown in the (v, w) phase plane. For the hard reset (left), perturbed trajectories (blue) converge to the limit cycle (red) immediately following the reset, at the reset point x_R. For the soft reset (right), the single perturbed trajectory converges slowly over several cycles. Parameters: $\lambda = 0.1$, $w_R = 1$, $v_R = 1$, $v_{eq} = -0.5$. For the soft reset, $w = 2.025$ was set to match the hard reset limit cycle, so that $w_0 = w_R$.
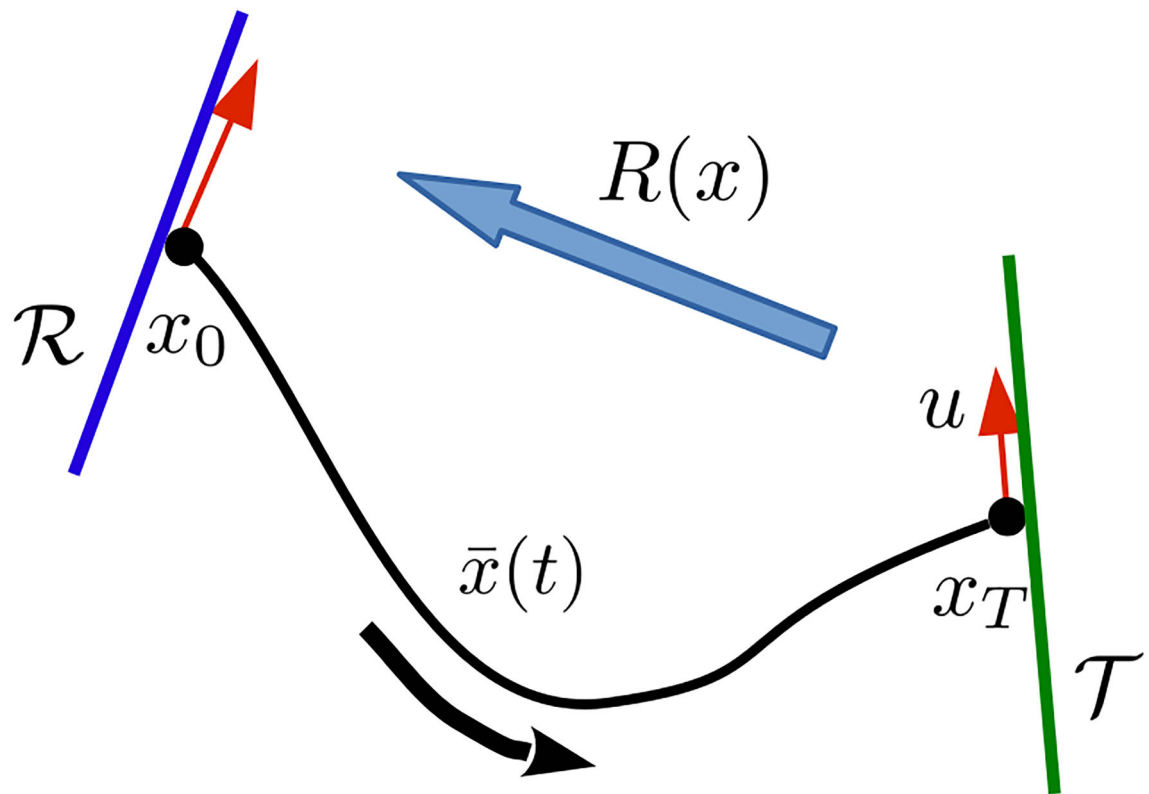
Figure 3.1.
Limit cycle trajectory $\bar{x}(t)$ evolves smoothly from initial condition x_0 on the reset manifold $\mathcal{R}$ to x_T on the threshold manifold $\mathcal{T}$, and then is returned by the reset map R(x) to $x_0 =$ R(x_T). A perturbation u along the threshold is mapped to a post-reset perturbation along the reset manifold.
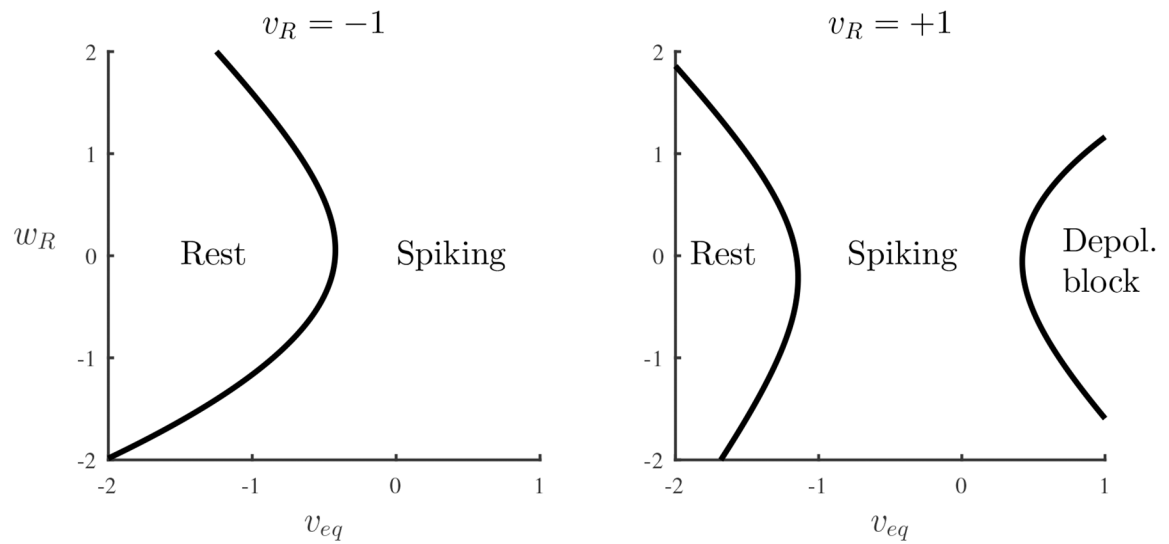
Figure 4.1.
Grazing bifurcations bounding the spiking regime in parameter space, for positive and negative reset regimes of the hard reset resonate-and-fire model with $\lambda = 0.1$. In both rest and depolarization block regimes, the system has a stable fixed point (quiescent state); this state is below threshold at rest and above threshold for depolarization block.
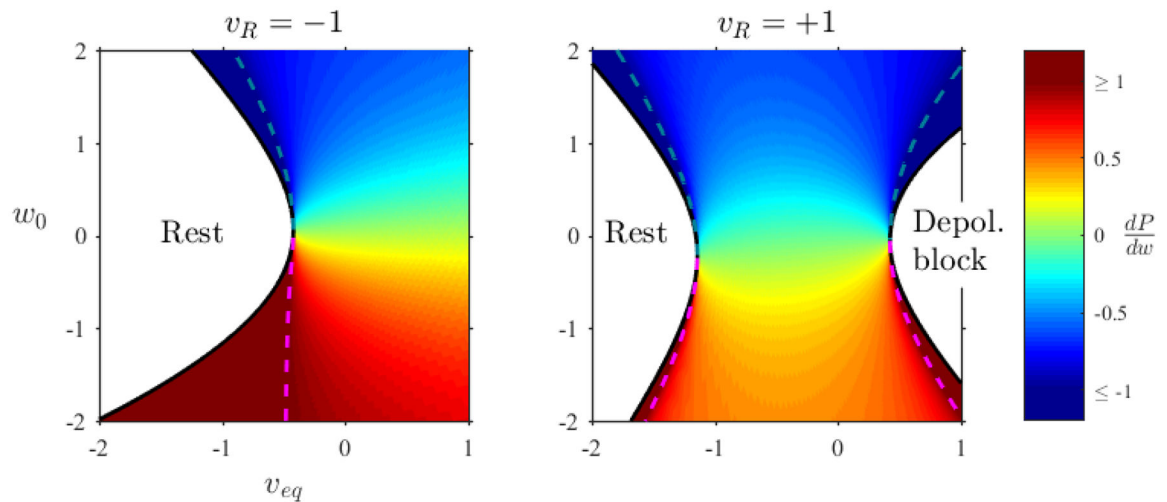
Figure 4.2.

Existence and stability of limit cycles for soft reset, for the negative reset (left), and positive reset (right) regimes. Color gives the stability quantified as the derivative of the return map P. Dashed lines show loss of stability, with blue-green the negative slope (period-doubling) and magenta the positive slope (saddle-node) bifurcation. Solid red/blue indicates unstable cycles past the bifurcation; slopes $\left|\frac{dP}{dw}\right| > 1$. Black lines show the grazing bifurcation of the unstable limit cycle. Parameters $\lambda = 0.1$ and $v_R = \pm 1$ are fixed while varying v_{eq} and w, plotted using w_0 to facilitate comparison with hard reset parameter space.
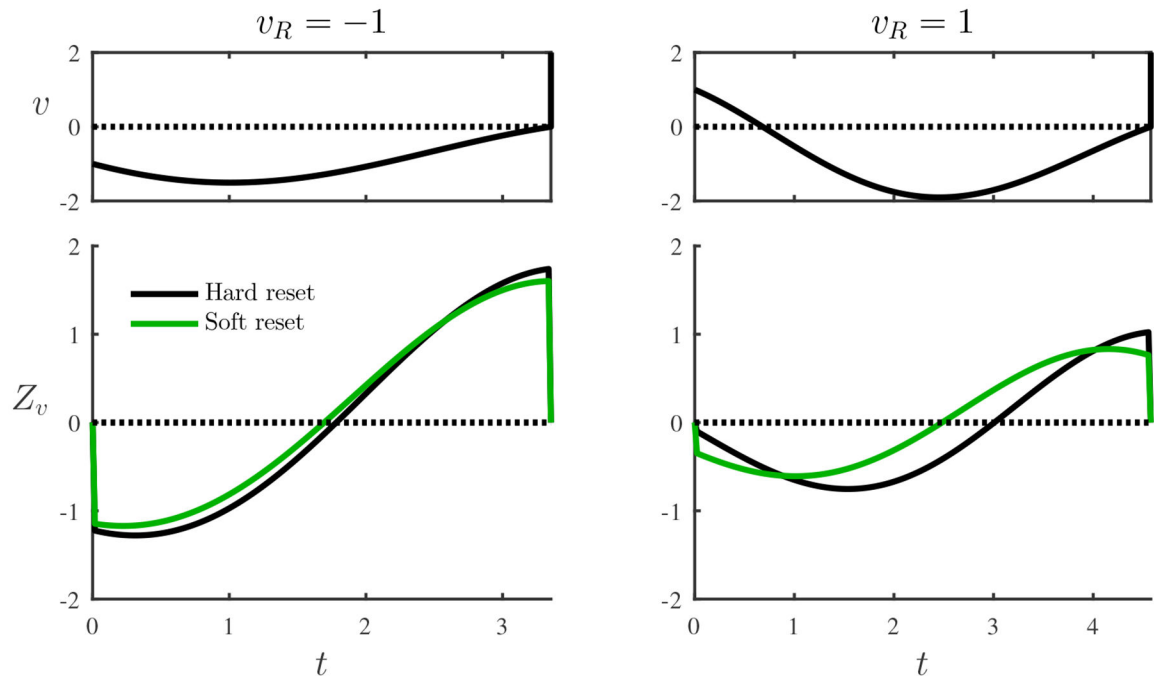
Figure 4.3.

The v-component PRC Z_v (t) (bottom), derived by the adjoint method for both soft and hard reset, shown along with the limit cycle v (t) (top) for reference. Parameters: $\lambda = 0.1$, $w_R = w_0 = 1$, $v_{eq} = -0.5$. For soft reset, $w = 2.025$ was set to match the hard reset limit cycle, so that $w_0 = w_R$.
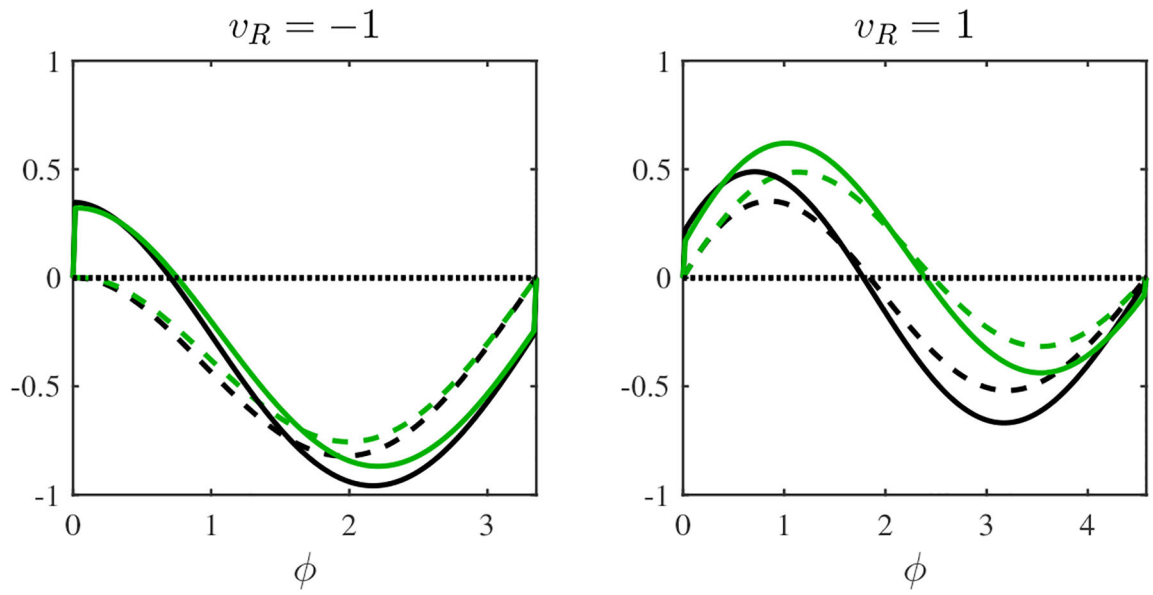
Figure 4.4.
Interaction function H including both spike and subthreshold contributions (solid lines), as well as subthreshold component H_{sub} (dashed), for the electrically coupled resonate-and-fire model with hard reset (black) and soft reset (green). Parameters: $\lambda = 0.1$, $w_R = 1$, $w = 2.025$, $v_{eq} = -0.5$, $M = 0.2$.
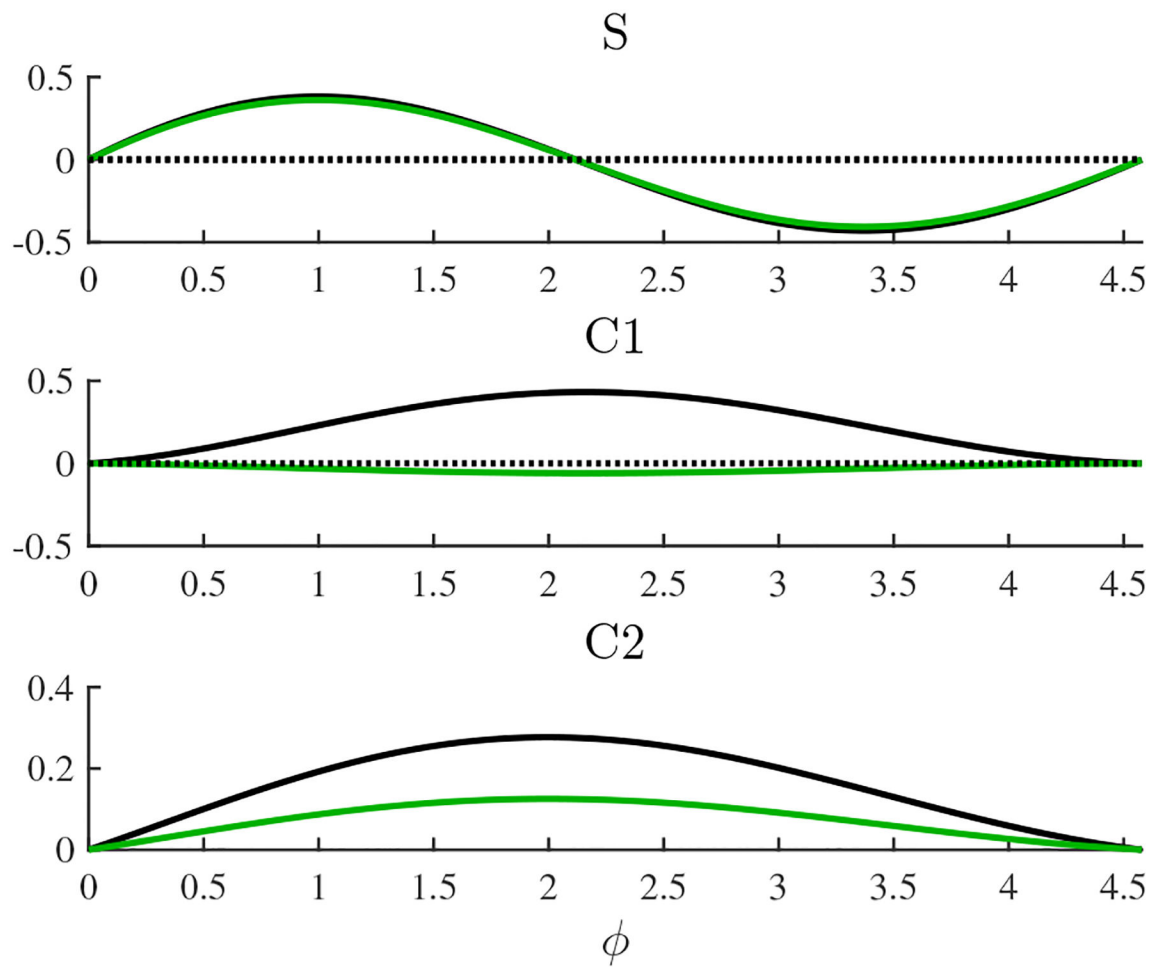
Figure 4.5.
Components of the subthreshold interaction function H_{sub} with approximate odd and even symmetry, for the electrically coupled resonate-and-fire model with hard reset (black) and soft reset (green). Parameters: $\lambda = 0.1$, $v_R = w_R = 1$, $w = 2.025$, $v_{eq} = -0.5$.
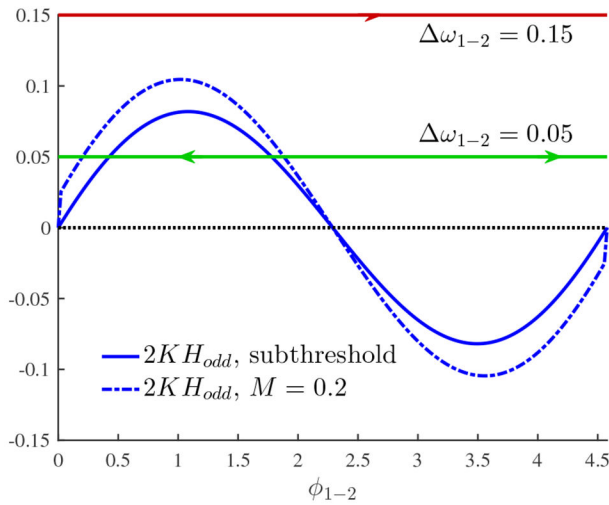
(a) Phase model fixed points   (b) Resonate-and-fire simulations
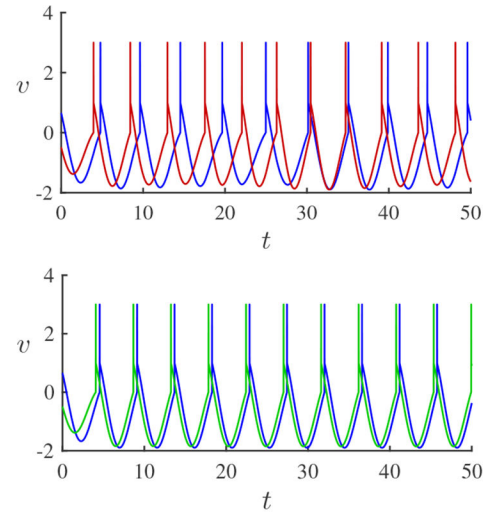
Figure 5.1.
Phase locking of a coupled pair. (a) Phase-locked states are fixed points of (5.2), intersections of $2KH_{odd}(\phi)$ (blue) with lines of constant frequency heterogeneity $\Delta\omega_{1-2}$ (red/green). Arrows give the flow of relative phase ϕ_{1-2}, indicating existence and stability of fixed points. The spiking component of H_{odd} provides additional robustness (dashed line with spike, solid line without). (b) Simulations show phase-locked (green) and phase walk-through (red) states corresponding to two levels of heterogeneity from A (subthreshold coupling only). Parameters: Hard reset, $\lambda = 0.1$, $w_R = 1$, $v_R = 1$, $v_{eq} = -0.5$, $M = 0$, $K = 0.1$.
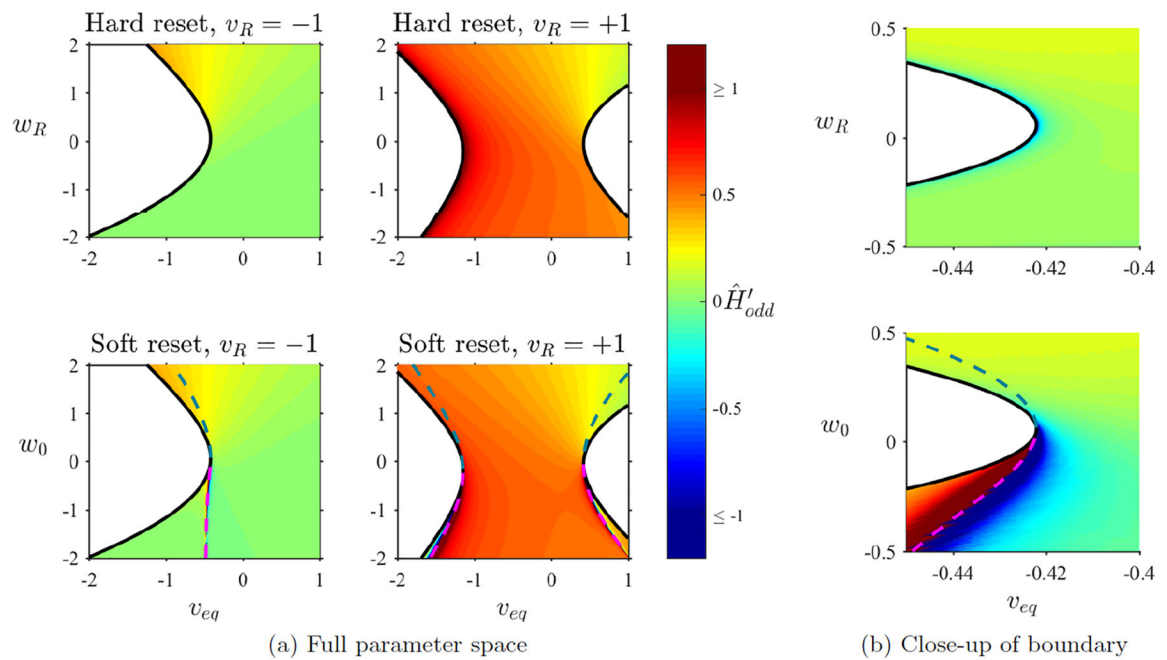
Figure 5.2.

Stability and robustness of synchrony. (a) Slope of $\widehat{H}_{odd}$, the odd component of the subthreshold interaction function, for $\lambda = 0.1$ as the equilibrium voltage (v_{eq}) and the reset coordinates (v_R and w_R or w_0) are varied. Magenta and cyan lines indicate stability boundaries of the limit cycle. (b) Expansion of left column (negative reset regime) near the spiking boundary.
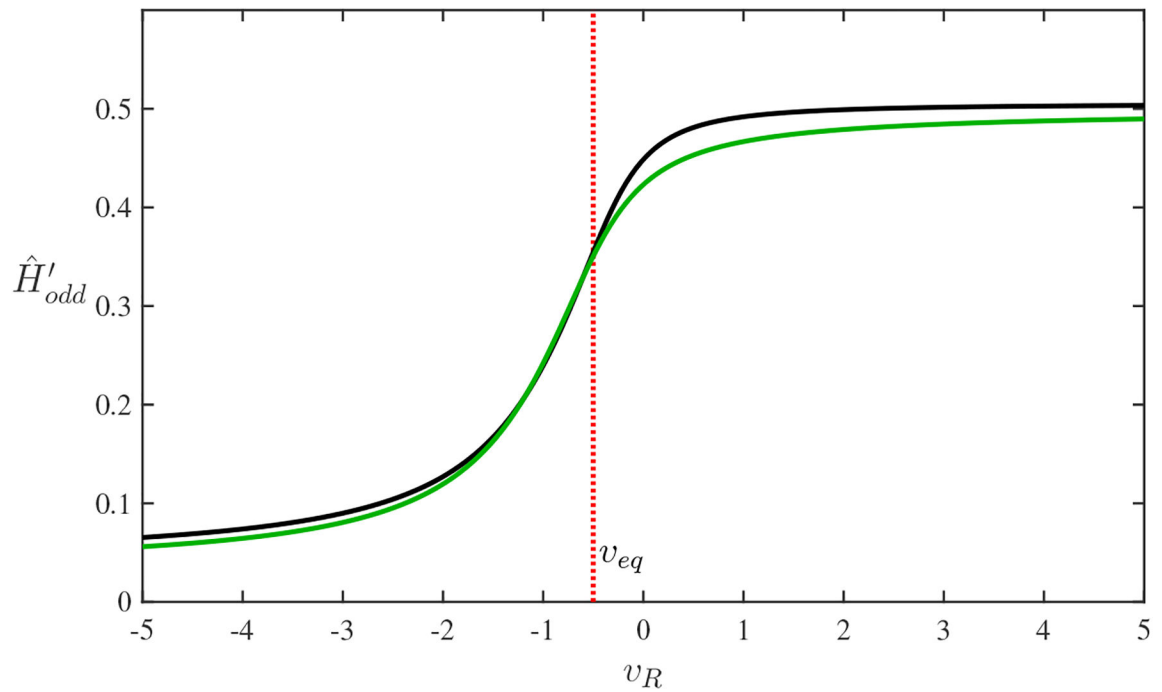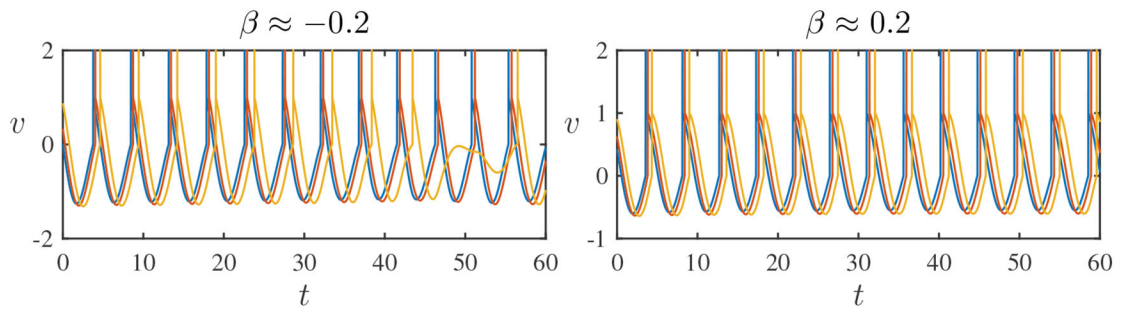
Figure 5.3.

Robustness of synchrony (as measured by the slope of $\widehat{H}_{odd}$) as the reset point v_R is varied between the AHP (negative extreme) and plateau potential (positive extreme) regimes. Hard reset shown in black; soft reset in green. Parameters: $\lambda = 0.1$, $w_R = 1$, $w = 2.025$, $v_{eq} = -0.5$.
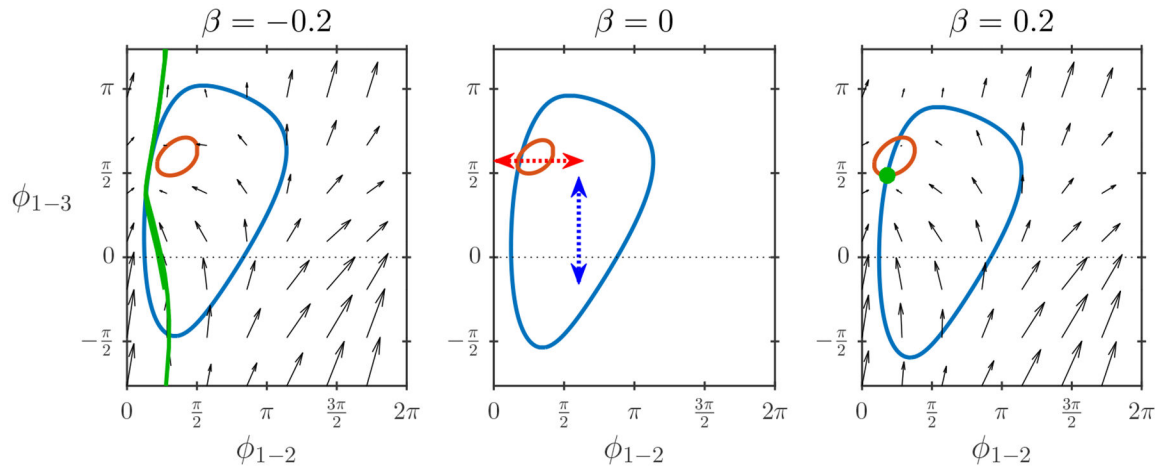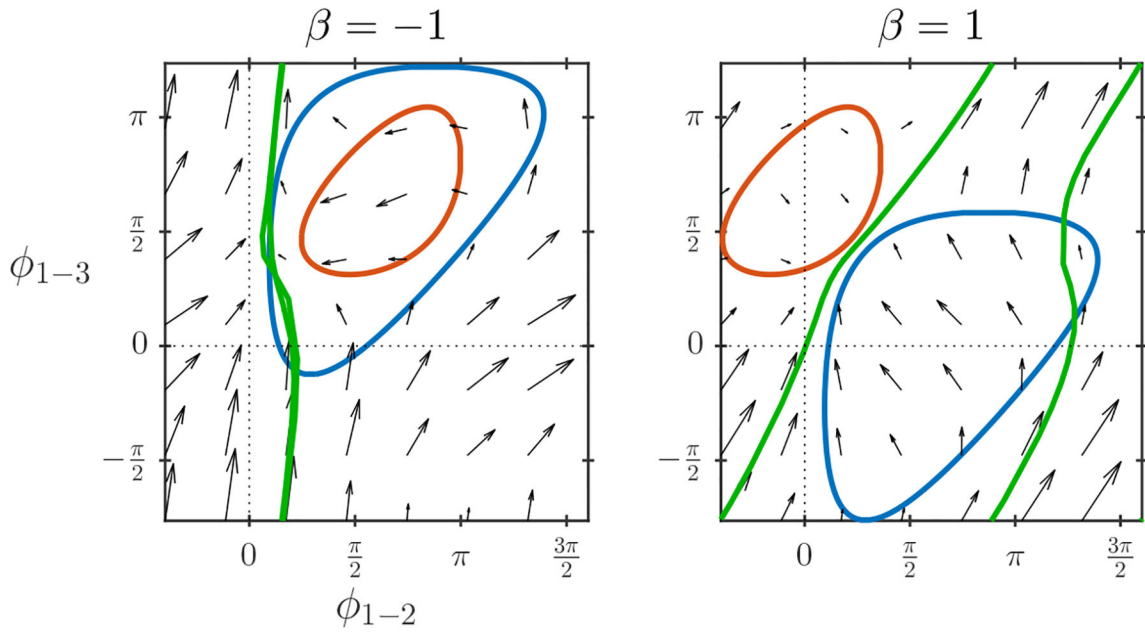
(a) Phase model nullclines

(b) Resonate-and-fire simulations

Figure 6.1.
Effect of a small even component on phase-locking of three-cell network. (a) Phase plane with nullclines of phase model (blue for ϕ_{1-2}; red for ϕ_{1-3}) at the critical coupling for existence of phase-locking with $\beta = 0$. The shift of nullclines eliminates the fixed point for negative β. Stable limit cycles and fixed points shown in green. (b) Simulations of the resonate-and-fire model show loss of fixed point with negative even component. Note that the phase-slipping oscillator (yellow) also misses a spike. Blue, red, and yellow denote oscillators 1, 2, and 3, respectively. Parameters: $W_i = (1.067, 1.017, 0.917)$, $k_{ij} = 0.09$ ($A_{odd} = 0.044$), $M = 0$, $\lambda = 0.1$, $v_R = 1$. For β positive/negative, respectively, $w_R = (0, 0.49)$, $v_{eq} = (-0.03, -0.3)$.
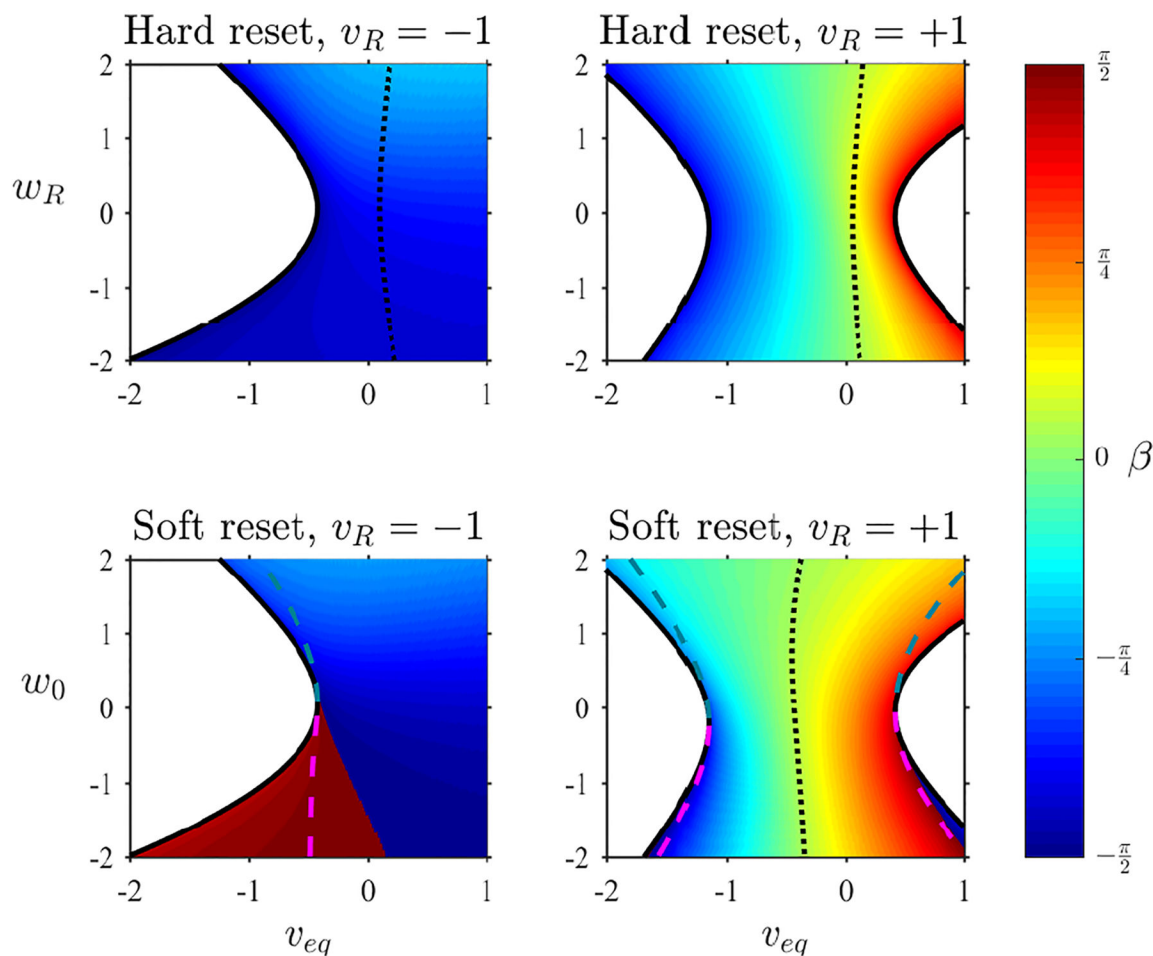
Figure 6.2.

Effect of a large even component on phase-locking of three-cell network. Nullclines of phase model (blue for ϕ_{1-2}; red for ϕ_{1-3}), at the critical coupling for existence of phase-locking with $\beta = 0$, are dramatically shifted and distorted for both large positive and negative even components, eliminating the fixed point in both cases. Stable limit cycles and fixed points shown in green: For $\beta = -1$ oscillators 1 and 2 are entrained, and for $\beta = 1$ oscillators 2 and 3 are entrained at a 1:2 frequency ratio. Parameters as in Figure 6.1.
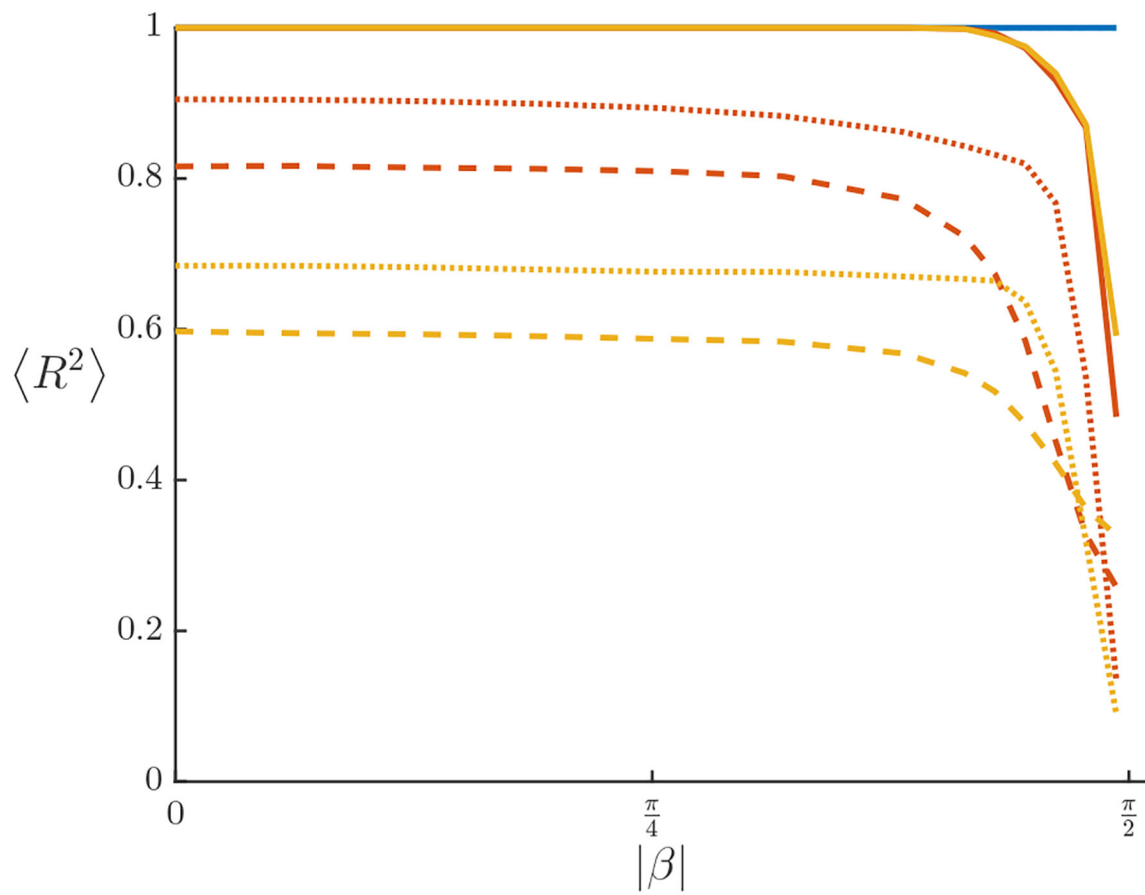
Figure 6.3.
Average level of synchrony R^2 for random three-cell networks decreases with increasing amplitude of even component. Note that $|\beta| = \frac{\pi}{2}$ is the limit of infinite even coupling. Dashed lines indicate both frequency and coupling heterogeneity; solid lines indicate coupling only; dotted lines indicate frequency only. Colors show level of heterogeneity. Frequencies are drawn from a Gaussian distribution (mean 0) and coupling weights from a log-normal distribution (mean 1), both with standard deviation $\sigma = 0, 1, 2$ for blue, red, yellow, respectively. Odd component of coupling fixed at $A_{odd} = 1$.

Figure 6.4.
Relative amplitude β of even to odd components of the electrically coupled resonate-and-fire subthreshold interaction function, from least-squares fit of H to the form (6.4) (for λ = 0.1, as the equilibrium voltage (v_{eq}) and the reset coordinates (v_R and w_R or w_0) are varied). Magenta and blue-green dashed lines indicate stability boundaries of the limit cycle for positive and negative slope instabilities. Dotted line indicates condition (6.6) for no reset-induced shear.